Multiple stellar populations in Magellanic Cloud clusters – VI. A survey of multiple sequences and Be stars in young clusters

A. P. Milone,[1,2]★ A. F. Marino,[2] M. Di Criscienzo,[3] F. D'Antona,[3] L. R. Bedin,[4]
G. Da Costa,[2] G. Piotto,[1,4] M. Tailo,[5] A. Dotter,[6] R. Angeloni,[7,8] J. Anderson,[9]
H. Jerjen,[2] C. Li,[10] A. Dupree,[6] V. Granata,[1,4] E. P. Lagioia,[1,11,12] A. D. Mackey,[2]
D. Nardiello[1,4] and E. Vesperini[13]

Affiliations are listed at the end of the paper

ABSTRACT

The split main sequences (MSs) and extended MS turnoffs (eMSTOs) detected in a few young clusters have demonstrated that these stellar systems host multiple populations differing in a number of properties such as rotation and, possibly, age. We analyse *Hubble Space Telescope* photometry for 13 clusters with ages between ∼40 and ∼1000 Myr and of different masses. Our goal is to investigate for the first time the occurrence of multiple populations in a large sample of young clusters. We find that all the clusters exhibit the eMSTO phenomenon and that MS stars more massive than ∼1.6 $\mathcal{M}_{\odot}$ define a blue and a red MS, with the latter hosting the majority of MS stars. The comparison between the observations and isochrones suggests that the blue MSs are made of slow-rotating stars, while the red MSs host stars with rotational velocities close to the breakup value. About half of the bright MS stars in the youngest clusters are Hα emitters. These Be stars populate the red MS and the reddest part of the eMSTO, thus supporting the idea that the red MS is made of fast rotators. We conclude that the split MS and the eMSTO are a common feature of young clusters in both Magellanic Clouds. The phenomena of a split MS and an eMSTO occur for stars that are more massive than a specific threshold, which is independent of the host-cluster mass. As a by-product, we report the serendipitous discovery of a young Small Magellanic Cloud cluster, GALFOR 1.

Key words: techniques: photometric – binaries: visual – stars: rotation – globular clusters: general – Magellanic Clouds.

1 INTRODUCTION

Recent studies, based on *Hubble Space Telescope* (*HST*) photometry, have revealed that the colour–magnitude diagram (CMD) of some ∼30–400 Myr old stellar clusters in the Large and Small Magellanic Clouds (LMC and SMC, respectively) exhibits either a broadened or a split main sequence (MS; Milone et al. 2013, Milone et al. 2015, Milone et al. 2016, 2017a; Bastian et al. 2017; Correnti et al. 2017; Li et al. 2017a). Moreover, most of these clusters show an extended MS turnoff (eMSTO), in close analogy with what is observed in nearly all the intermediate-age (∼1–2 Gyr old) clusters of both Magellanic Clouds (e.g. Bertelli et al. 2003; Mackey & Broby Nelsen 2007; Glatt et al. 2008; Milone et al. 2009). These findings have challenged the traditional picture that the CMDs of young and intermediate-age star clusters are best described by simple isochrones and have triggered huge efforts to understand the physical reasons responsible for the double MSs and the eMSTOs.

The comparison between the observed CMDs of young clusters and stellar models shows that the split MS is consistent with two stellar populations with different rotation rates: a red MS, which hosts stars with rotational velocities close to the breakup value, and a blue MS, which is made of slow-rotating or non-rotating stars (D'Antona et al. 2015; Milone et al. 2016; Bastian et al. 2017). It is well known that B-type stars with Hα emission (Be stars) are fast rotators (see the review by Rivinius, Carciofi & Martayan 2013). As a consequence, the

★ E-mail: antonino.milone@unipd.it

existence of fast-rotating stars in young clusters is further supported by the presence of a large number of Be stars (e.g. Keller et al. 1998; Bastian et al. 2017; Correnti et al. 2017) and by direct spectroscopic measurements of rotational velocities in MS stars (Dupree et al. 2017).

While the interpretation of the split MS is widely accepted, the physical reasons responsible for the eMSTO are still controversial. The most straightforward interpretation for the eMSTO is that young and intermediate-age clusters have experienced a prolonged star formation and host multiple generations with different ages (Mackey et al. 2008; Goudfrooij et al. 2011, 2014; Correnti et al. 2014; Piatti & Cole 2017). The evidence that the CMDs of both young Magellanic Cloud clusters and old globular clusters (GCs) are not consistent with a single isochrone has suggested that the clusters with eMSTO could be the young counterparts of old GCs with multiple populations (e.g. Conroy et al. 2011; Keller, Mackey & Da Costa 2011).

As an alternative, it has been suggested that the eMSTO is another consequence of the presence of populations with different rotation rates (Bastian & de Mink 2009; Yang et al. 2011, 2013; Li, de Grijs & Deng 2014; D'Antona et al. 2015; Niederhofer et al. 2015). This would be consistent with the inferred picture for young clusters, but it seems that stellar models with different rotation rates alone are not able to entirely reproduce the observations and some age spread is still required (e.g. Correnti et al. 2017; Goudfrooij, Girardi & Correnti 2017; Milone et al. 2017a). D'Antona et al. (2017) have noticed that the blue MS of the studied young clusters hosts a subpopulation of stars, which seems younger than the majority of blue-MS stars. They suggested that stars caught in the stage of braking from a rapidly rotating configuration are responsible for this feature of the CMD, and that these stars mimic an $\sim$30 per cent younger stellar population now.

In this work, we derive high-precision *HST* photometry to investigate homogeneously the multiple populations and H α-emitting stars in 13 clusters of both Magellanic Clouds younger than $\sim$1 Gyr. Our sample comprises both clusters that have not been investigated in the context of multiple populations, namely KRON 34, NGC 294, NGC 1801, and NGC 1953, and clusters with previous evidence of multiple sequences in the CMD. The latter include NGC 330, NGC 1755, NGC 1805, NGC 1818, NGC 1850, NGC 1856, NGC 1866, NGC 1868, and NGC 2164 (Li et al. 2014, 2017; Correnti et al. 2015, 2017; Milone et al. 2015, Milone et al. 2016, Milone et al. 2017). This paper is organized as follows. In Section 2, we describe the data and the data reduction, and present the CMDs in Section 3. The MS and the eMSTO are first investigated in Section 4, while Section 5 compares the observed CMDs with stellar models. In Section 6, we derive the fraction of stars in the distinct MSs of each cluster, while Section 7 is dedicated to stars with H α emission. Finally, a summary and a discussion are provided in Section 8.

2 DATA AND DATA ANALYSIS

The data set of this paper is mostly collected as part of our programmes GO 13379, GO 14204, and GO 14710. Multiband images of 3 SMC clusters and 10 LMC clusters were obtained through the Ultraviolet and VISual channel of the Wide-Field Camera 3 (UVIS/WFC3) on board *HST*. We used images in the *F336W* and *F814W* bands for all the analysed clusters, whereas *F656N* images are available for all the targets but NGC 1755 and NGC 1866. In addition, we exploited *F225W* data of NGC 330, NGC 1805, NGC 1818, and NGC 2164 and *F275W* images of NGC 1850. Details on the data are provided in Table 1.

Stellar astrometry and photometry have been carried out by using the flt images and the procedure and the computer programs developed by one of us (JA). In a nutshell, we first removed the effect of the poor charge-transfer efficiency (CTE) of UVIS/WFC3 by using the empirical pixel-based method by Anderson & Bedin (2010) and derived for each image a 5×5 array of perturbation point spread functions (PSFs). To do this, we used a library array of empirical PSFs plus a spatially varying array of PSF residuals that we obtained from unsaturated bright and isolated stars.

We followed two distinct approaches to measure stars with different luminosities. All the bright stars have been measured in each image separately, by using the derived PSFs and the program IMG2XYM_WFC3UV, which is similar to the Wide-Field Camera package IMG2XYM_WFC by Anderson & King (2006) but for UVIS/WFC3. This software routine also identifies saturated stars and estimates their fluxes and positions. In particular, it determines the amount of flux from the bled-into pixels, thus allowing an accurate flux determination for each saturated star (see Gilliland 2004; Anderson et al. 2008; Gilliland, Rajan & Deustua 2010). Faint stars have been measured by using a software package from Anderson et al. (in preparation), which analyses all the images together to derive the stellar fluxes and luminosities. It is an improved version of the program by Anderson et al. (2008), and we refer to papers by Sabbi et al. (2016) and Bellini et al. (2017) for details on the method.

Stellar positions have been corrected for the effect of geometric distortion by using the solution from Bellini, Anderson & Bedin (2011) and have been transformed into the *Gaia* DR1 reference frame (Gaia Collaboration et al. 2016). Only relatively isolated stars that are well fitted by the PSF and have a small rms scatter in the position measurements have been included in the following analysis. The sample of stars with high-quality photometry has been selected by using the procedure described in Milone et al. (2009) and the various diagnostics of the astrometric and photometric quality provided by the computer programs.

As an example of a typical cluster, we show in Fig. 1 the trichromatic image of the analysed field of NGC 2164.[1] The inner circle has been derived by eye with the criteria of selecting a region that is mostly populated by cluster members. It will be called the cluster field, hereafter. The analysis of each cluster is based on stars in the cluster field, while in forthcoming papers of this series we will investigate the radial distribution of multiple populations in close analogy with what we have done in Milone et al. (2016) and Li et al. (2017b). Nevertheless, we verified that the main conclusions of this work are not affected by the choice of the cluster field. The region outside the azure circle

---

[1] The stacked images of all the clusters are available at http://progetti.dfa.unipd.it/GALFOR/

Table 1. Description of the data used in this paper.

Cluster	Date	Camera	Filter	$N \times$ exposure time	GO	PI
KRON 34	2017, Jan, 13	UVIS/WFC3	*F814W*	90 s + 680 s	14710	A. P. Milone
	2017, Jan, 13	UVIS/WFC3	*F656N*	2×720 s	14710	A. P. Milone
	2017, Jan, 13	UVIS/WFC3	*F336W*	3×839 s	14710	A. P. Milone
NGC 294	2017, Feb, 08	UVIS/WFC3	*F814W*	90 s+680 s	14710	A. P. Milone
	2017, Feb, 08	UVIS/WFC3	*F656N*	2×720 s	14710	A. P. Milone
	2017, Feb, 08	UVIS/WFC3	*F336W*	3×839 s	14710	A. P. Milone
NGC 330	2017, Jul, 03	UVIS/WFC3	*F814W*	90 s+680 s	14710	A. P. Milone
	2017, Jul, 03	UVIS/WFC3	*F656N*	2×720 s	14710	A. P. Milone
	2015, Jul, 26	UVIS/WFC3	*F336W*	10 s+100 s+805 s+3 ×960 s	13727	J. Kalirai
	2015, Jul, 26	UVIS/WFC3	*F225W*	10 s+100 s+5 ×950 s	13727	J. Kalirai
NGC 1755	2015, Oct, 05–Dec, 28 – 2016, Mar, 26–Jun, 10	UVIS/WFC3	*F814W*	4×90 s+4 ×678 s	14204	A. P. Milone
	2015, Oct, 05–Dec, 28 – 2016, Mar, 26–Jun, 10	UVIS/WFC3	*F336W*	8×711 s	14204	A. P. Milone
NGC 1801	2017, Feb, 26	UVIS/WFC3	*F814W*	90 s+666 s	14710	A. P. Milone
	2017, Feb, 26	UVIS/WFC3	*F656N*	2×720 s	14710	A. P. Milone
	2017, Feb, 26	UVIS/WFC3	*F336W*	2×834 s+835	14710	A. P. Milone
NGC 1805	2017, Oct, 06	UVIS/WFC3	*F814W*	90 s+666 s	14710	A. P. Milone
	2017, Oct, 06	UVIS/WFC3	*F656N*	2×720 s	14710	A. P. Milone
	2015, Oct, 28	UVIS/WFC3	*F336W*	10 s+100 s+790 s+3 ×947 s	13727	J. Kalirai
	2015, Oct, 28	UVIS/WFC3	*F225W*	10 s+100 s+5 ×938 s	13727	J. Kalirai
NGC 1818	2017, Feb, 03	UVIS/WFC3	*F814W*	90 s+666 s	14710	A. P. Milone
	2017, Feb, 03	UVIS/WFC3	*F656N*	2×720 s	14710	A. P. Milone
	2015, Oct, 29	UVIS/WFC3	*F336W*	10 s+100 s+790 s+3 ×947 s	13727	J. Kalirai
	2015, Oct, 29	UVIS/WFC3	*F225W*	10 s+100 s+5 ×938 s	13727	J. Kalirai
NGC 1850	2015, Oct, 22	UVIS/WFC3	*F814W*	7 s+350 s+440 s	14174	P. Goudfrooij
	2015, Oct, 22	UVIS/WFC3	*F656N*	900 s+925 s+950 s	14174	P. Goudfrooij
	2015, Dec, 19	UVIS/WFC3	*F336W*	260 s+370 s+600 s+650 s+675 s	14069	N. Bastian
	2015, Oct, 22	UVIS/WFC3	*F275W*	150 s+780 s+790 s	14174	P. Goudfrooij
NGC 1856	2013, Nov, 12	UVIS/WFC3	*F814W*	51 s+360 s+450 s	13011	P. Goudfrooij
	2014, Feb, 09–Mar, 24 – May, 18–Jun, 11	UVIS/WFC3	*F814W*	4×90 s+4 ×704 s	13379	A. P. Milone
	2013, Nov, 12	UVIS/WFC3	*F656N*	735 s+2 ×940 s	13011	P. Goudfrooij
	2014, Feb, 09–Mar, 24 – May, 18–Jun, 11	UVIS/WFC3	*F336W*	8×711 s	13379	A. P. Milone
NGC 1866	2016, Mar, 01–May, 31 – Jun, 01–Aug, 18	UVIS/WFC3	*F814W*	4×90 s+4 ×678 s	14204	A. P. Milone
	2016, Mar, 01–May, 31 – Jun, 01–Aug, 18	UVIS/WFC3	*F336W*	8×711 s	14204	A. P. Milone
NGC 1868	2016, Dec, 16	UVIS/WFC3	*F814W*	90 s+666 s	14710	A. P. Milone
	2016, Dec, 16	UVIS/WFC3	*F656N*	2×720 s	14710	A. P. Milone
	2016, Dec, 16	UVIS/WFC3	*F336W*	830 s+2 ×831 s	14710	A. P. Milone
NGC 1953	2017, Jul, 18	UVIS/WFC3	*F814W*	90 s+666 s	14710	A. P. Milone
	2017, Jul, 18	UVIS/WFC3	*F656N*	2×720 s	14710	A. P. Milone
	2017, Jul, 18–19	UVIS/WFC3	*F336W*	2×834 s+835 s	14710	A. P. Milone
NGC 2164	2017, Feb, 02	UVIS/WFC3	*F814W*	90 s+758 s	14710	A. P. Milone
	2017, Feb, 02	UVIS/WFC3	*F656N*	2×720 s	14710	A. P. Milone
	2015, Sep, 05–06	UVIS/WFC3	*F336W*	10 s+100 s+790 s+3 ×947 s	13727	J. Kalirai
	2015, Sep, 05	UVIS/WFC3	*F225W*	10 s+100 s+5 ×938 s	13727	J. Kalirai

plotted in Fig. 1 has the same area as the cluster field but is mostly populated by field stars and defines the reference field. It will be used to statistically estimate the contamination of field stars in the cluster field.

The cluster-field radii, R_{cf}, that we adopted for each cluster are provided in Table 2, where we also indicate the host Magellanic Cloud, the coordinates of the cluster centre, the mass, the age, the distance modulus, and the reddening. The masses for the majority of clusters have been derived by McLaughlin & van der Marel (2005) by assuming a Wilson (1975) profile. In the cases of NGC 1755, NGC 1801, and NGC 1953, which are not included in the sample analysed by McLaughlin & van der Marel, we used the masses from Popescu, Hanson & Elmegreen (2012). Unfortunately, no mass estimates are available for Kron 34 and NGC 294. All the remaining parameters listed in Table 2 are derived in this paper. The cluster centres have been estimated as in Li et al. (2017a) by using the contours of the number density of stars brighter than $m_{F814W} = 22.0$. Ages, distances, and reddenings have been derived by comparing isochrones from the Geneva data base with the observed CMDs (see Section 5 for details).

2.1 Differential reddening

A significant spatial variation of the reddening across the field of view results in a broadening of the stellar colours and the magnitudes in the CMD, and we may need to correct the photometry for the effect of differential reddening in order to properly investigate multiple populations.

To estimate the differential reddening suffered by each star, we applied the method of Milone et al. (2012) to all the analysed GCs. Briefly, we first derived the absorption coefficient in the filters available in this paper as in Milone et al. (2016). To do this, we simulated a
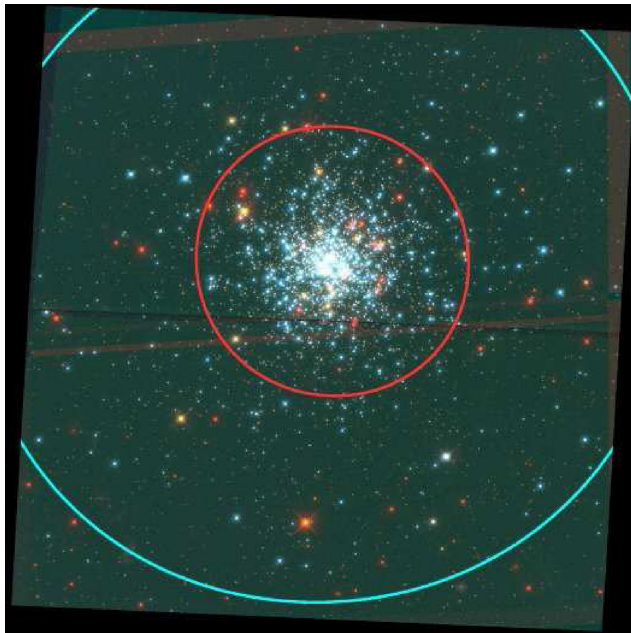
Figure 1. Three-colour image of NGC 2164. The regions within the red circle and outside the azure circle are indicated as the cluster field and reference field, respectively.

Table 2. Parameters of the studied clusters. Masses of NGC 1755, NGC 1801, and NGC 1953 are from Popescu et al. (2012), while the masses of the other clusters are taken from McLaughlin & van der Marel (2005) by assuming a Wilson (1975) profile. The remaining cluster parameters are derived in this paper.

Cluster	Galaxy	RA (J2000)	Dec. (J2000)	$\log(\mathcal{M}/\mathcal{M}_\odot)$	Age (Myr)	$(m-M)_0$	$E(B-V)$	R_{cf} (arcsec)
KRON 34	SMC	00 55 33.50	−72 49 56.0	—	630	18.80	0.08	20
NGC 294	SMC	00 53 04.94	−73 22 45.7	—	500	18.80	0.15	22
NGC 330	SMC	00 56 18.59	−72 27 48.1	4.61	40	18.80	0.11	24
NGC 1755	LMC	04 55 15.53	−68 12 16.8	3.60	80	18.35	0.13	32
NGC 1801	LMC	05 00 34.57	−69 36 46.2	4.26	315	18.40	0.16	28
NGC 1805	LMC	05 02 21.73	−66 06 42.6	3.70	50	18.40	0.10	20
NGC 1818	LMC	05 04 13.42	−66 26 03.1	4.41	40	18.40	0.10	48
NGC 1850	LMC	05 08 45.20	−68 45 38.7	5.04	80	18.35	0.15	40
NGC 1856	LMC	05 09 30.21	−69 07 44.4	5.07	250	18.30	0.19	20
NGC 1866	LMC	05 13 38.77	−65 27 51.4	4.91	200	18.30	0.12	32
NGC 1868	LMC	05 14 35.80	−63 57 14.0	4.34	1000	18.45	0.09	40
NGC 1953	LMC	05 25 28.07	−68 50 16.5	4.20	250	18.40	0.18	24
NGC 2164	LMC	05 58 55.89	−68 30 57.5	4.18	100	18.35	0.13	36

synthetic spectrum, for a star with metallicity $Z = 0.006$, effective temperature $T_{\rm eff} = 13\,285$ K, and gravity $\log g = 4.29$, by using the ATLAS12 and SYNTHE codes (Kurucz 2005; Sbordone, Bonifacio & Castelli 2007). According to the isochrones from Georgy et al. (2014), the adopted atmospheric parameters correspond to an MS star of NGC 1755 with $m_{F814W} = 19.1$ (see Milone et al. 2016 for details). The simulated spectrum, which includes the wavelength interval between 1900 and 10 000 Å, has been convolved over the transmission curves of the filters used in this paper by assuming the reddening law by Cardelli, Clayton & Mathis (1989) to derive the following absorption coefficients: $A_{F225W} = 8.25\,E(B-V)$, $A_{F275W} = 6.38\,E(B-V)$, $A_{F336W} = 5.16\,E(B-V)$, $A_{F656N} = 2.165\,E(B-V)$, and $A_{F814W} = 2.04\,E(B-V)$. Moreover, we obtained $A_B = 4.27\,E(B-V)$ and $A_V = 3.27\,E(B-V)$.

To estimate the amount of differential reddening affecting each star, we first determined the direction of reddening vector in the m_{F814W} versus $m_{F336W} - m_{F814W}$ plane by using the above-mentioned values of the absorption coefficients, and rotated the CMD into a reference frame where the abscissa is parallel to that direction. We then derived the ridge line of the red MS and selected a sample of reference red-MS stars that have high-quality photometry and astrometry according to the criteria of selection described in Section 2. Finally, we calculated for each star the colour residuals of the 50 nearest reference stars with respect to the red-MS ridge line. We converted the median of the colour residual into the best estimate for the differential reddening, $\Delta E(B - V)$, while the corresponding error has been derived from the ratio between the rms of the 50 colour-residual measurements and the square root of 49.

The procedure for the determination of the differential reddening across the field of view of each cluster is based only on the m_{F814W} versus $m_{F336W} - m_{F814W}$ CMD in most clusters. As exceptions, in NGC 330, NGC 1805, NGC 1818, and NGC 2164, we used the average

$\Delta E(B - V)$ values inferred from the m_{F814W} versus $m_{F336W} - m_{F814W}$ and m_{F814W} versus $m_{F225W} - m_{F814W}$ CMDs. In the case of NGC 1850, we combined information from the m_{F814W} versus $m_{F336W} - m_{F814W}$ and m_{F814W} versus $m_{F275W} - m_{F814W}$ CMDs.

The inferred values of $\Delta E(B - V)$ associated with the stars of most clusters, namely NGC 294, NGC 330, NGC 1755, NGC 1801, NGC 1805, NGC 1818, NGC 1866, NGC 1868, NGC 1953, and NGC 2164, are typically $\sim$0.003 mag and are comparable to the measurement errors, which are around 0.003 mag. This fact indicates that the reddening is almost constant across the field of view and that any reddening variation is either comparable or smaller than our photometric uncertainties. In these cases, the CMD corrected for differential reddening is almost indistinguishable from the original CMD, and we will use the latter to analyse the multiple stellar populations. KRON 34, NGC 1850, and NGC 1856 are the only clusters with significant variations of reddening across the field of view (see also Correnti et al. 2015, 2017; Milone et al. 2015 for NGC 1850 and NGC 1856). In the following, we will analyse the differential-reddening-corrected CMDs of these three clusters.

2.2 Artificial stars

Artificial-star (AS) tests have been used to estimate the photometric errors and the completeness level of our sample and have been run by using the procedure described by Anderson et al. (2008). Briefly, we first produced for each cluster a list of 300 000 stars with instrumental magnitudes from −4.0, which is below the detection limit of the data, to the saturation limit in the *F814W* band and calculated the corresponding *F336W* and *F656N* magnitudes by using the fiducial line of the MS and the MSTO derived from the observed CMD. In the cases of NGC 330, NGC 1805, NGC 1818, and NGC 2164, we included in the AS list only the *F225W* magnitude, and in the case of NGC 1850, we included the stellar magnitudes in the *F275W* band. At this stage, we used the instrumental magnitudes that are defined as $-2.5\log_{10}(\text{flux})$, where the flux is provided in photoelectrons and is recorded to the reference exposure.

ASs have been generated with a flat luminosity function in the *F814W* band. We included in the list the stellar coordinates in the reference frame and assumed for ASs a spatial distribution that resembles the observed spatial distribution of stars brighter than $m_{F814W} = 20.0$. We emphasize here that since ASs are used to estimate completeness and photometric errors, the adopted luminosity function and spatial distribution do not affect the results. The AS tests were performed for one star at a time and entirely in the software so that the ASs would never interfere with each other. For each AS in the input list, we added the star to each exposure with the appropriate flux and position and measured it by following the same method as used for real stars. We considered a star as recovered if the input and the output positions differed by less than 0.5 pixel and the fluxes by less than 0.75 mag. Moreover, we included in our analysis only ASs that had passed the criteria of selection that we had adopted for real stars.

Photometric errors depend on stellar luminosity and on crowding. To infer the typical uncertainty associated with the magnitude of a star, we selected all the ASs with the same luminosity, within 0.1 mag, and with the same radial distance from the cluster centre, within 200 WFC3/UVES pixels. The error is estimated as the 68.27th percentile of the distribution of the absolute values of the difference between the measured magnitude and the input magnitude of the selected stars.

To calculate the completeness value associated with each star, we divided the WFC3/UVIS field of view into five concentric annuli centred on the cluster centre, and, within each of them, we analysed the ASs in 15 magnitude intervals, from −4 to the saturation level. We derived the average completeness corresponding to each of these grid points by calculating the fraction of the recovered to input artificial stars within that bin. The completeness value associated with each star has been derived by linearly interpolating among the grid points.

3 THE COLOUR–MAGNITUDE DIAGRAMS

Figs 2–6 provide a collection of CMDs for stars in the cluster field (black points) and in the reference field (aqua crosses). Specifically, the left-hand and the right-hand panels show the m_{F814W} versus $m_{F336W} - m_{F814W}$ and m_{F814W} versus $m_{F656N} - m_{F814W}$ diagrams, respectively, while middle panels are zoom-ins of the CMDs plotted on the left-hand panels. In the cases of NGC 1755 and NGC 1866, for which there are no *F656N* data available, we plot the m_{F814W} versus $m_{F336W} - m_{F814W}$ CMD only. The clusters are sorted by age from youngest ($\sim$40 Myr, NGC 330) to oldest ($\sim$1 Gyr, NGC 1868).

The left-hand and middle panels show that all the clusters exhibit the eMSTO. Moreover, the upper MS, above the kink at $m_{F814W} \lesssim$ 20.5–21.5, is typically split into a blue and a red sequence. The single exception is the oldest cluster NGC 1868 (Fig. 6), which does not show a split MS. In this cluster, the faintest part of the eMSTO is only slightly brighter than the magnitude of the MS kink.

All the clusters exhibit a well-populated sequence of binary stars that is clearly visible on the red side of the red MS, and will be the subject of a forthcoming paper of this series. In this context, NGC 330 is an intriguing case where a populous sequence of binaries seems to cross the red MS around $m_{F814W} \sim 18.5$.

We plot in the right-hand panels of Figs 2–6 the m_{F814W} versus m_{F656N}–m_{F814W} CMDs for stars in the cluster field, and notice that both the MS and the MSTO define a nearly-vertical sequence. The CMDs of the five youngest clusters, namely NGC 330, NGC 1818, NGC 1805, NGC 1850, and NGC 2164, also display a cloud of bright stars that are significantly bluer than the bulk of MS stars and that span a wide range of $m_{F656N} - m_{F814W}$ colours. These stars, which populate the upper MS only and disappear below $m_{F814W} \sim 18.5$, are marked with red crosses in Figs 2–6. This reveals that the stars with an excess of *F656N* luminosity mostly populate the eMSTO and the red MS in the m_{F814W} versus $m_{F336W} - m_{F814W}$ CMD. Their $m_{F656N} - m_{F814W}$ and $m_{F336W} - m_{F814W}$ colour distributions dramatically change from one cluster to another.
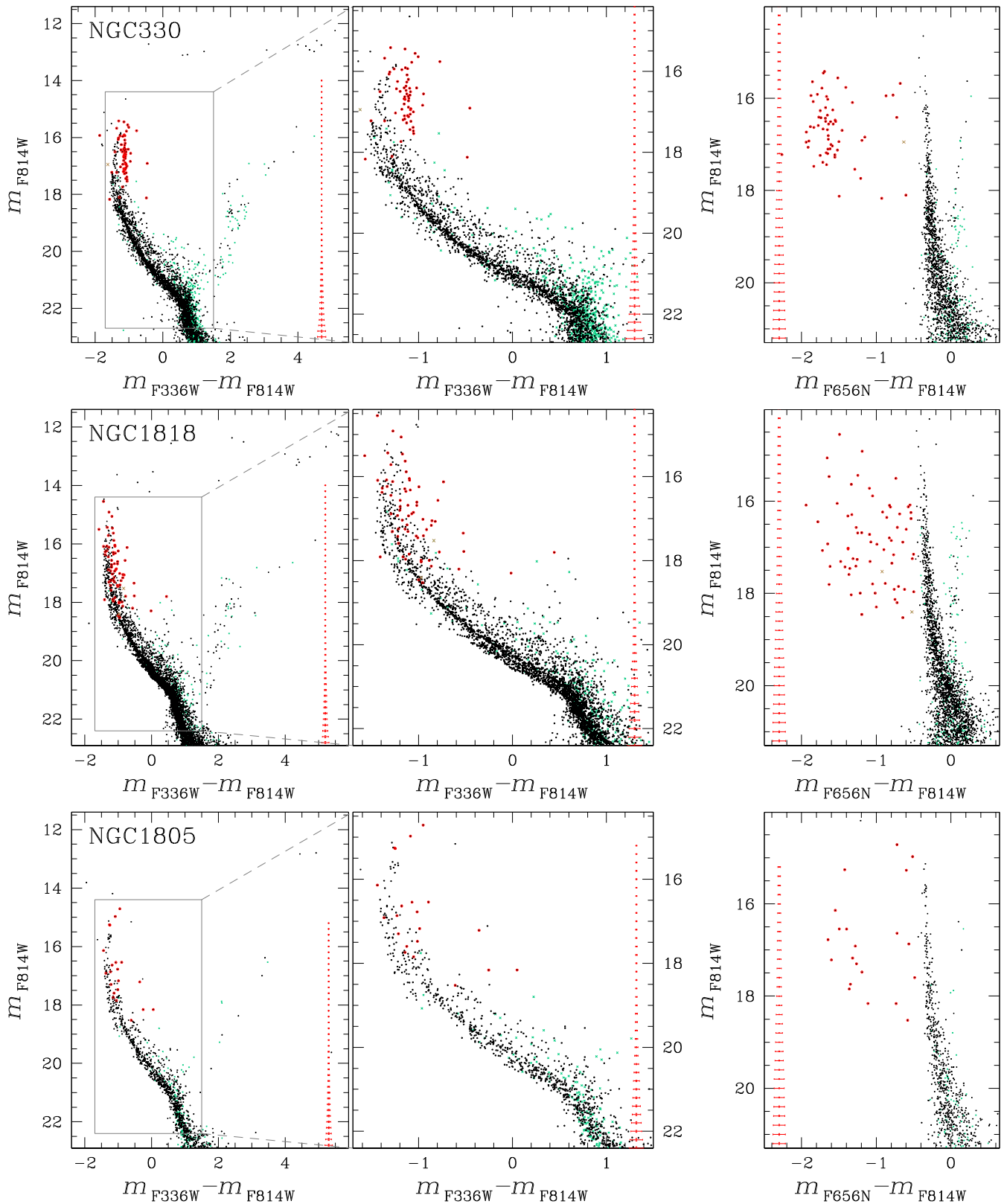
Figure 2. Collection of CMDs for stars in the field of view of NGC 330, NGC 1818, and NGC 1805. The left-hand panels show the m_{F814W} versus $m_{F336W} - m_{F814W}$ CMD for stars in the cluster field (black points) and in the reference field (aqua crosses). The middle panels are a zoom-in of the left-hand-panel CMDs around the upper MS and the MSTO. The right-hand panels plot m_{F814W} against $m_{F656N} - m_{F814W}$ for stars in the cluster field (black points) and in the reference field (aqua crosses). Candidate H α emitters in the cluster field and in the reference field have been selected in the right-hand-panel CMDs and are represented with red circles and brown crosses, respectively, in all the diagrams of this figure. The clusters are sorted in order of increasing age.
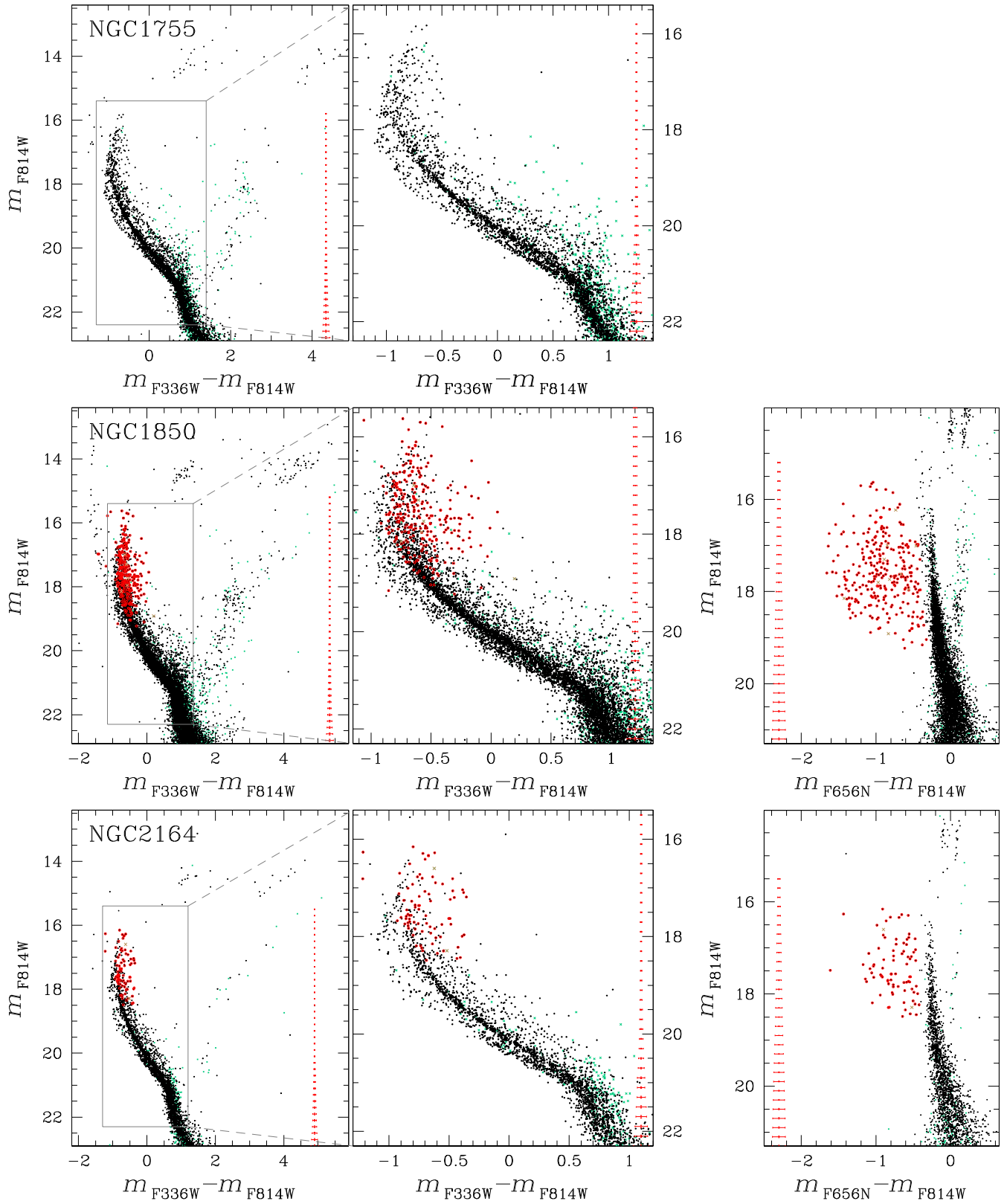
Figure 3. As in Fig. 2 but for NGC 1755, NGC 1850, and NGC 2164. Photometry in the *F656N* band is not available for NGC 1755.
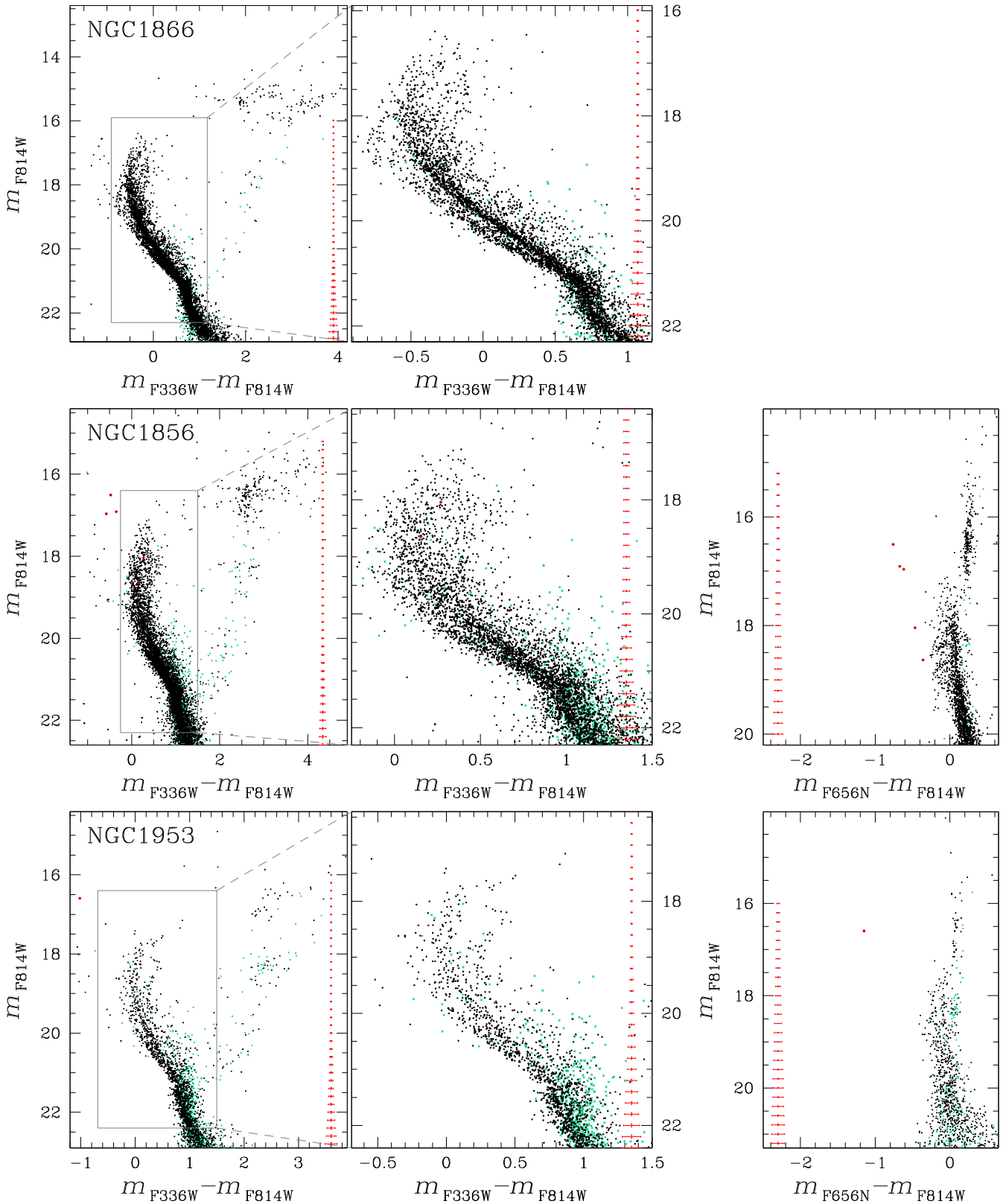
Figure 4. As in Fig. 2 but for NGC 1866, NGC 1856, and NGC 1953. Photometry in the *F656N* band is not available for NGC 1866.
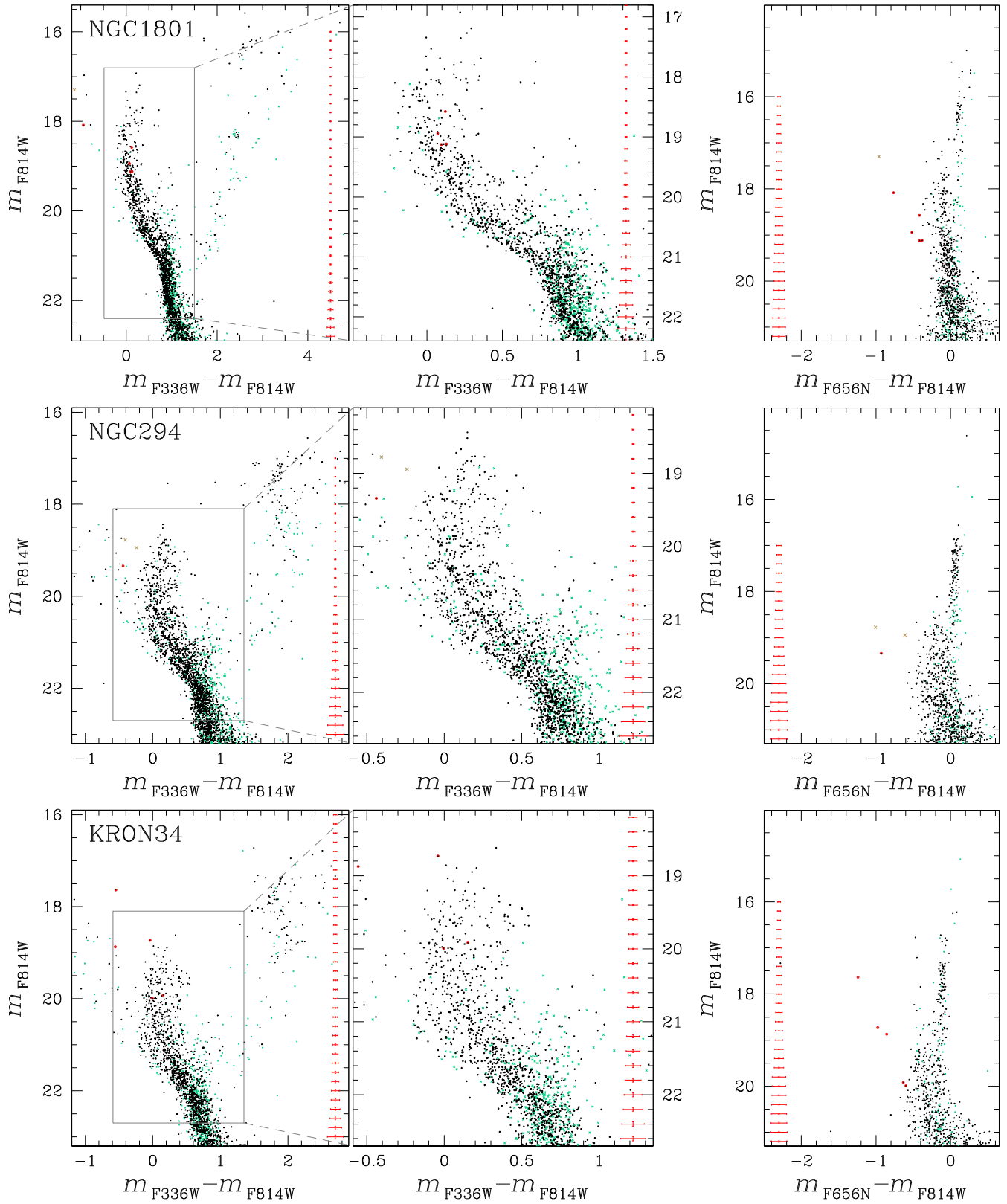
Figure 5. As in Fig. 2 but for NGC 1801, NGC 294, and KRON 34.
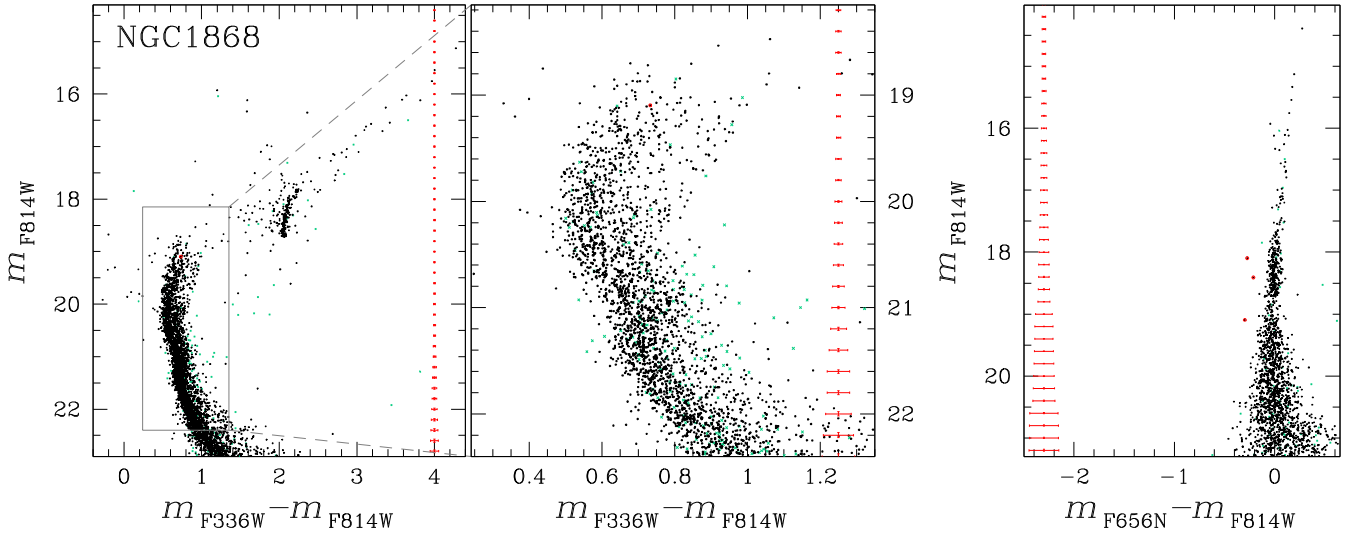
Figure 6. As in Fig. 2 but for NGC 1868.

Our results are consistent with previous findings by Keller, Bessell & Da Costa (2000) based on the Wide Field Planetary Camera 2 *F160BW*, *F555W*, and *F656N* imaging of NGC 330 in the SMC, and three young LMC clusters: NGC 1818, NGC 2004, and NGC 2100. Keller and collaborators found that these clusters host a large fraction of Be stars and discovered that Be stars have redder *F160BW* − *F555W* colours than the majority of MS stars.

In addition to *F336W*, *F656N*, and *F814W* data, the *HST* archive includes UVIS/WFC3 images in *F225W* of NGC 330, NGC 1805, NGC 1818, and NGC 2164 and *F275W* images of NGC 1850. We have defined the pseudo-magnitudes $m_{F336W, F225W, F814W} = m_{F336W} - m_{F225W} + m_{F814W}$ and $m_{F336W, F275W, F814W} = m_{F336W} - m_{F275W} + m_{F814W}$ and plotted these pseudo-magnitudes against $m_{F336W} - m_{F814W}$. The CMDs are shown in Fig. 7 for stars in the fields of NGC 330, NGC 1805, NGC 1818, and NGC 2164, and in Fig. 8 for NGC 1850. These diagrams confirm the split MSs and eMSTOs and provide a better separations between blue-MS and red-MS stars than the m_{F814W} versus $m_{F336W} - m_{F814W}$ CMDs.

4 THE SPLIT MS AND THE EXTENDED MSTO

In this section, we demonstrate that the split MSs and the eMSTOs are not due to contamination by foreground and background stars. To do this, we applied to each cluster, the procedure illustrated in Fig. 9 for NGC 2164. In panels (a1) and (b1), we compared the m_{F814W} versus $m_{F336W} - m_{F814W}$ CMD of stars in the cluster field zoomed in around the upper MS and the corresponding CMD for a stars in the reference field, which has the same area as the cluster field. Due to the small field of view of UVIS/WFC3, we can assume that the field stars have nearly the same distribution in the CMD of the cluster field and the reference field. In this case, the fraction of field stars in the cluster-field CMD and in the range of colour and magnitude populated by MS stars with $m_{F814W} < 22.0$ and $(m_{F336W} - m_{F814W}) < 1.2$ is typically smaller than 0.1 and ranges from 0.05 in NGC 1866 to 0.26 in NGC 1801.

To quantify the contamination of non-cluster members in the cluster-field CMD, we statistically subtracted the reference-field CMD from the cluster-field CMD in close analogy with what we have done in the previous papers of this series. Briefly, for each star, i, in the cluster-field CMD, we defined a distance in the CMD given by

$$d_i = \sqrt{k[(m_{F336W,cf} - m_{F814W,cf}) - (m^i_{F336W,rf} - m^i_{F814W,rf})]^2 + (m_{F814W,cf} - m^i_{F814W,rf})^2},$$

where $m_{F336W(F814W), cf}$ and $m_{F336W(F814W), rf}$ are the *F336W* (*F814W*) magnitudes in the cluster field and reference field, respectively. The value of the constant $k = 4.1$, which has been introduced by Gallart et al. (2003) to account for the fact that the colour of a star is better constrained than its magnitude, has been calculated as in Marino et al. (2014, see their section 3.1).

For each star in the reference field, we considered the star in the cluster-field CMD with the smallest distance to each star of the reference field as the candidate to be subtracted. The star, i, in the reference field and the closest star in the cluster field have different completeness levels (c^i_{rf} and c^i_{cf}). To account for this fact, we generated a random number r_i between 0 and 1 and subtracted from the cluster-field CMD all the candidates with $r_i < c^i_{rf}/c^i_{cf}$.

Results are illustrated in panels (c1) and (d1) of Fig. 9, where we show the decontaminated CMD and the CMD of the subtracted stars. The fact that both the split MSs and the eMSTOs are visible in the decontaminated CMD demonstrates that they are intrinsic features of the cluster CMD.

We applied the same method to statistically subtract field stars from the m_{F814W} versus $m_{F656N} - m_{F814W}$ cluster-field CMDs. The adopted procedure, which is illustrated in panels (a2)–(d2) of Fig. 9 for NGC 2164, has been applied to all the clusters and demonstrates that the vast majority of stars with H α excess are cluster members.
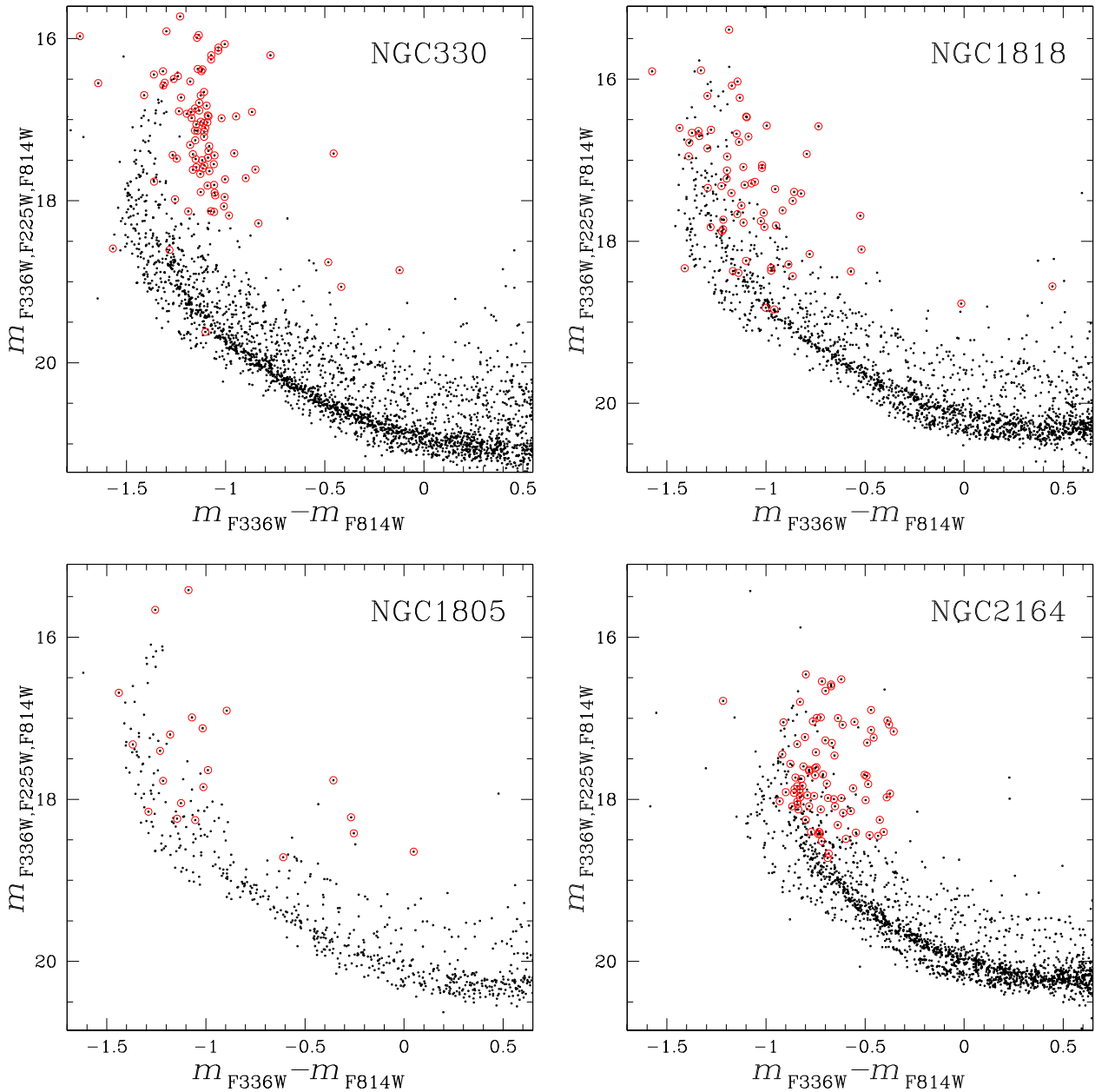
Figure 7. $m_{F336W, F225W, F814W} = m_{F336W} - m_{F225W} + m_{F814W}$ versus $m_{F336W} - m_{F814W}$ diagrams for NGC 330, NGC 1818, NGC 1805, and NGC 2164. Red circles mark candidate stars with H α emission.

5 COMPARISON WITH THEORY

A number of papers in the literature have shown that the red MS of young Magellanic- Cloud clusters can be explained with a population of rapidly rotating stars with a rotation rate close to the breakup value, ω_c, while the blue MS could be composed of slow-rotating or non-rotating stars (D'Antona et al. 2015; Milone et al. 2016, Milone et al. 2017a; Bastian et al. 2017; Correnti et al. 2017 ; Li et al. 2017a). The interpretation of the eMSTO is still debated, and it is not clear whether an age variation, together with a range of stellar rotation, is needed to reproduce the observations (e.g. Goudfrooij et al. 2017).

To further investigate the physical reasons that are responsible for the eMSTO and the split MS, we used the isochrones from the Geneva and Padova data bases (Bressan et al. 2012; Mowlavi et al. 2012; Ekström et al. 2013; Georgy et al. 2014; Marigo et al. 2017). Specifically, we compared the observed CMDs with isochrones with different ages and different rotation rates in close analogy with what we have done in previous papers of this series. We assumed that the stars have the same helium abundance. Indeed we have already demonstrated that the observed split MS and the eMSTO are inconsistent with multiple populations with different helium abundances (Milone et al. 2016). Moreover, we assumed that the stars are chemically homogeneous, as suggested by spectroscopic and photometric studies of NGC 419, NGC 1806, NGC 1846, and NGC 1866 (Mucciarelli et al. 2011, 2014; Mackey et al., in preparation; Martocchia et al. 2017; Milone 2017).
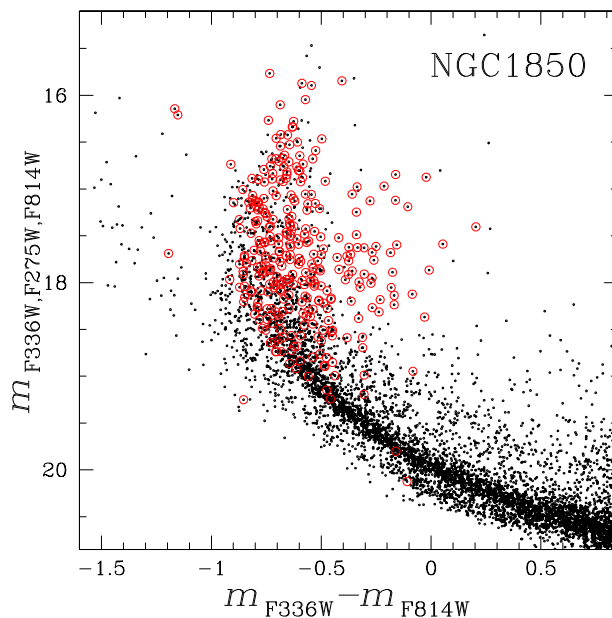
Figure 8. $m_{F336W, F275W, F814W} = m_{F336W} - m_{F275W} + m_{F814W}$ versus $m_{F336W} - m_{F814W}$ diagram for NGC 1850. Red circles mark candidate stars with Hα emission.
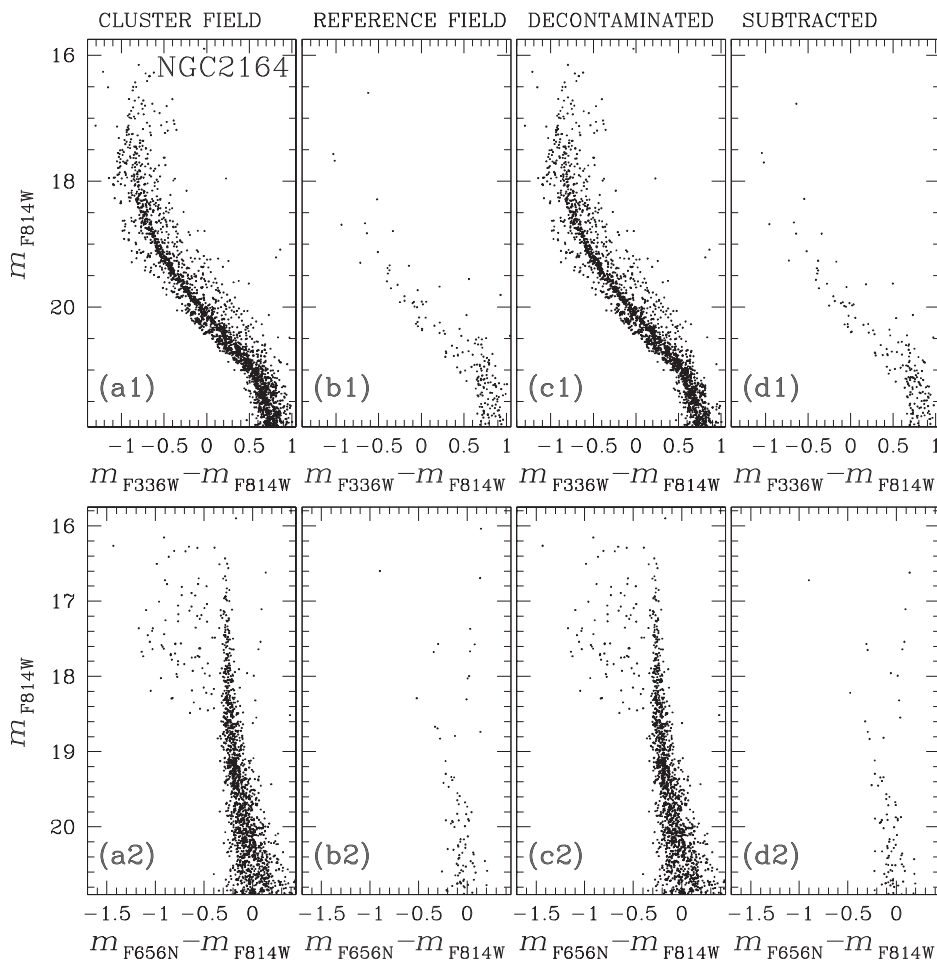

Figure 9. This figure illustrates the procedure to statistically subtract field stars from the cluster-field CMDs of NGC 2164. The upper and lower panels refer to the m_{F814W} versus $m_{F336W} - m_{F814W}$ and m_{F814W} versus $m_{F656N} - m_{F814W}$ CMDs, respectively. Panels (a1) and (a2) show the CMDs of stars in the cluster field, while the CMDs of stars in the reference field are plotted in panels (b1) and (b2). The decontaminated CMDs are shown in panels (c1) and (c2), while the subtracted stars are plotted in panels (d1) and (d2). See text for details.
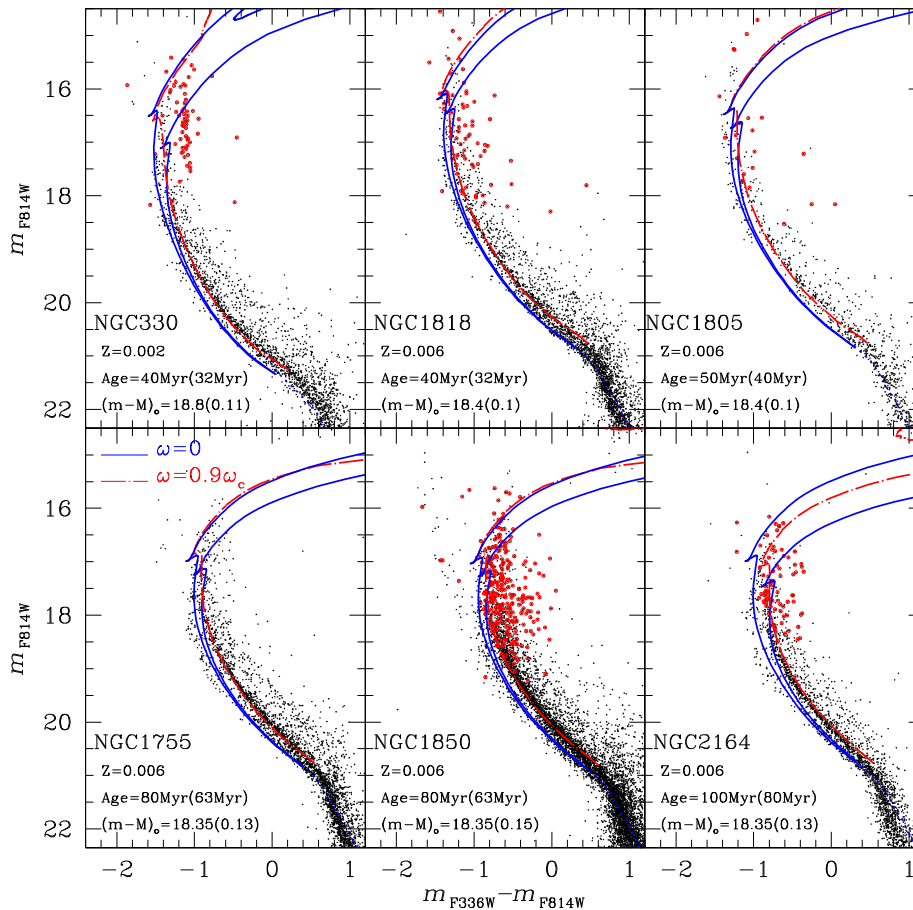
Figure 10. Comparison between isochrones (Bertelli et al. 2012; Ekström et al. 2013; Georgy et al. 2014; Marigo et al. 2017) and the observed CMDs of NGC 330, NGC 1818, NGC 1805, NGC 1755, NGC 1850, and NGC 2164. Blue and red lines represent non-rotating isochrones and isochrones with $\omega = 0.9\omega_c$ (Ekström et al. 2013; Georgy et al. 2014). In each panel, we quoted the adopted values for the age of the red isochrones, the intrinsic distance modulus, the reddening (in brackets), and the metallicity. The blue isochrones with the faintest MSTO have the same age as the red isochrone, while the ages of the youngest blue isochrones are indicated in each panel (in brackets). The dotted-blue lines are the non-rotating isochrones from Mowlavi et al. (2012) and Bertelli et al. (2012) that we used to reproduce the lower MS.

The adopted values for distance modulus [$(m - M)_0$], reddening [$E(B - V)$], and ages, which provide the best fit between the observations and the isochrones, are provided in Table 2. We assumed metallicities of $Z = 0.002$ and 0.006, for SMC and LMC clusters, respectively. The adopted reddening has been converted into absorption in the *F336W* and *F814W* bands by using the coefficients derived in Section 2.1.

Results are illustrated in Figs 10–12, where we have superimposed on each CMD the corresponding best-fitting isochrones. We find that the blue and red MSs of all clusters are consistent with two coeval populations of non-rotating or slowly rotating stars and of stars with a high rotation rate ($\omega = 0.9\omega_c$), which we have coloured blue and red, respectively.

All the clusters younger than $\sim$650 Myr (12/13) host a significant number of bright stars on the blue side of the upper MS. As noticed in previous work (e.g. D'Antona et al. 2017; Milone et al. 2017a), these stars are consistent with slow rotators and are reproduced by the bluest isochrones that are younger than the other isochrones. The age difference between the two blue isochrones is quoted in each figure.

As previously noticed for NGC 1856, NGC 1755, and NGC 1866 (D'Antona et al. 2015; Milone et al. 2016, Milone et al. 2017a), the comparison between the observed CMDs and the isochrones is not fully satisfactory, as the faint eMSTO is poorly reproduced by the models. In principle, we could improve the fit by assuming that the rotating population spans a range of ages. However, we note that the poor quality of the fit could be due to uncertainties in the isochrones. As noticed by D'Antona et al. (2015), the models of the core-hydrogen-burning phase may be affected by several second-order parameters, including the effect of the inclination angle and the calculation of stellar luminosity and effective temperature.

Since models from Ekström et al. (2013) and Georgy et al. (2014) are available only for bright stars, we used non-rotating isochrones from other works (blue-dotted lines in Figs 10–12) to reproduce the lower MS of the analysed clusters. For LMC clusters, we used isochrones from the Geneva group, which are available only for a metallicity of $Z = 0.006$ (Mowlavi et al. 2012), while for the SMC clusters we used isochrones from the Padova data base (Bressan et al. 2012; Marigo et al. 2017).

We expect that the non-rotating isochrones would overlap the fast-rotating ones at the luminosity of the MS kink, a feature previously observed in the CMDs of Galactic open clusters, which indicates the onset of envelope convection due to the opacity peak of partial hydrogen ionization (e.g. D'Antona et al. 2002).
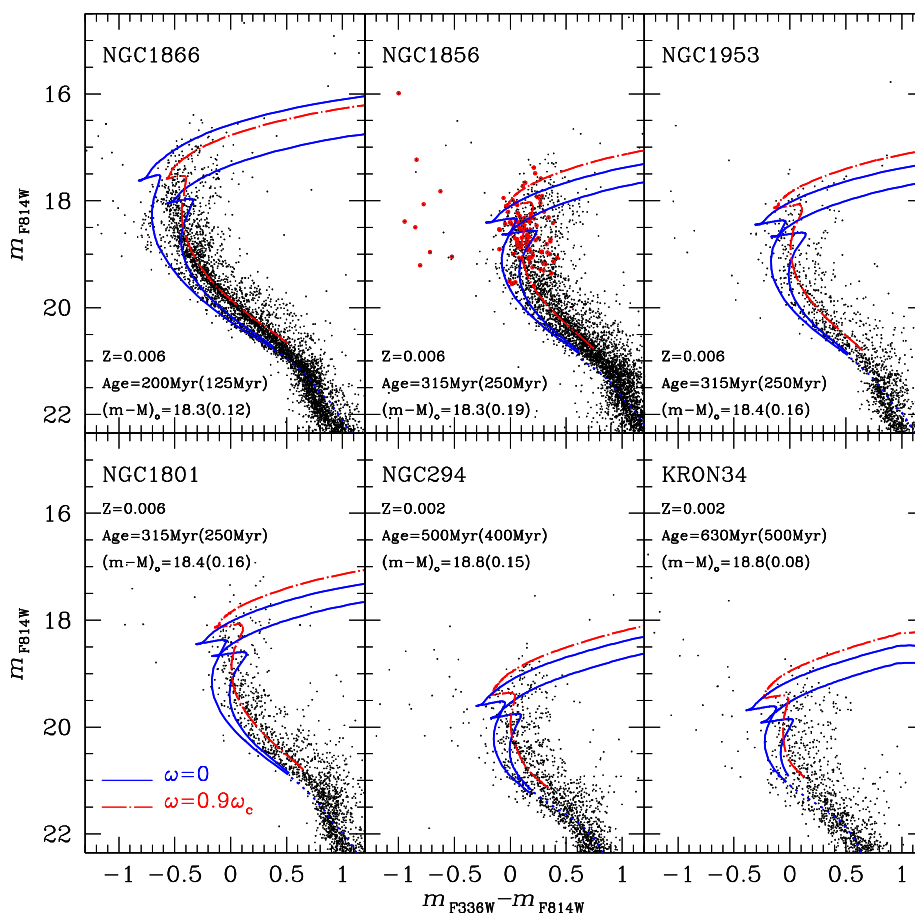
Figure 11. As in Fig. 10 but for NGC 1866, NGC 1856, NGC 1953, NGC 1801, NGC 294, and KRON 34.
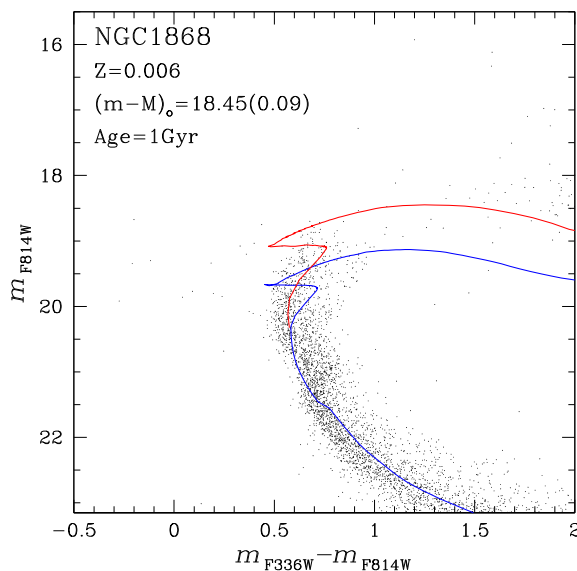

Figure 12. Comparison between isochrones from the Geneva data base and the observed CMD of NGC 1868. The non-rotating isochrone and the isochrone with $\omega = 0.9\omega_c$ are coloured blue and red, respectively. The adopted values for the age, distance modulus, reddening, and metallicity are quoted in the figure.

Stars above the MS kink, which are present only in young clusters and belong to the spectral classes A and B, are hotter than $\sim$7500 K and are characterized by radiative envelopes. Rapidly rotating A and B MS stars are $\lesssim$300 K colder than slowly rotating stars with the same luminosity and distribute along the blue and red MSs. In contrast, the envelopes of stars fainter than the MS kink are convective. Even though their cores might still be rapidly rotating, the effective-temperature differences between rapid rotators and non-rotators with the same luminosity become much smaller and so the sequences effectively merge in the CMD.
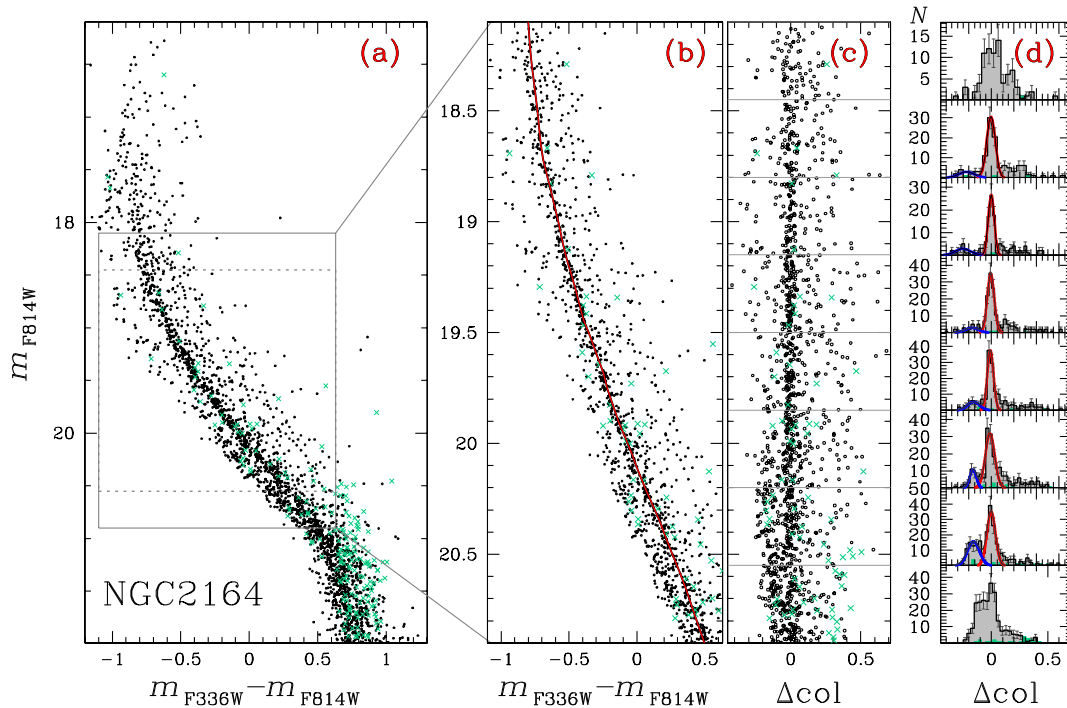
Figure 13. This figure illustrates the procedure that we used to estimate the fraction of blue- and red-MS stars with respect to the total number of MS stars in NGC 2164. Panel (a) reproduces the m_{F814W} versus $m_{F336W} - m_{F814W}$ CMD of Fig. 3, while panel (b) is a zoom-in of the CMD region where the MS split is more prominently visible. The red line overplotted on the CMD is the fiducial line of the red MS. Panel (c) shows the verticalized m_{F814W} versus Δcol diagram for the stars plotted in panel (b). Finally, panels (d) show the histogram distribution of Δcol for stars in eight intervals of *F814W* magnitude. The red and blue lines overimposed on the six central histograms are the components of the best-fitting bi-Gaussian function of each histogram. We did not fit with a function the uppermost and the lowermost histograms, which correspond to MS stars above and below the two dotted lines in the left-hand panel. See text for details.

The fact that the fast-rotating and the non-rotating MSs merge together around the kink is predicted by the MIST isochrones (Dotter 2016; Choi et al. 2016), and is consistent with what we observe in the CMDs where the blue and red MSs cross and get very close to each other at the same luminosity.

6 POPULATION RATIO

To determine the fraction of blue-MS and red-MS stars with respect to the total number of MS stars, we used a procedure that is based on the analysis of the m_{F814W} versus $m_{F336W} - m_{F814W}$ CMD and has been adopted in the previous papers of this series. This procedure has been applied to all the clusters but NGC 1868, which is the oldest object in our sample and shows no evidence for a split MS.

The method is illustrated in Fig. 13 for NGC 2164. We analysed only the MS region within the grey rectangle shown in the CMD plotted in panel (a), where the split MS is more clearly visible. We derived the fiducial line of the red MS plotted on the CMD shown in panel (b). To derive the fiducial, we divided a sample of red-MS stars selected by eye into bins of 0.2 mag, which are defined over a grid of points separated by steps of 0.05 mag (Silverman 1986). For each bin, we calculated the median of the colours and magnitudes of all the stars in that bin. These median points were smoothed with the boxcar averaging method, which replaces each point with the average of the three adjacent points.

The verticalized m_{F336W} versus Δcol diagram plotted in panel (c) of Fig. 13 has been derived by subtracting from the $m_{F336W} - m_{F814W}$ colour of each star the colour of the red fiducial line corresponding to the same magnitude in the *F814W* band. We defined eight intervals of 0.25 mag each, and the Δcol histogram distributions of the stars in the various bins are plotted in panels (d) of Fig. 13.

Most histograms exhibit a bimodal Δcol distribution, which we fitted with a bi-Gaussian function. The two components of the best-fitting least-squares Gaussians are represented with the blue and red lines overplotted on the histograms of Fig. 13. To minimize the effect of binary stars, we excluded from the fit all the stars with Δcol larger than 0.08. The areas under the blue and red histograms are used to infer the ratio between blue- and red-MS stars in each magnitude bin.

The two MSs of NGC 2164 merge together at $m_{F814W} \sim 20.8$. As a consequence, we did not use the bi-Gaussian function to fit the histogram distribution plotted in the lower panel. Above $m_{F814W} \sim 18.5$, some MS stars evolve to the red side of the MS. For this reason, we did not estimate the population ratio of the stellar populations in the upper bin.

In addition to the procedure described above, Milone et al. (2017a) used a more sophisticated method to infer the relative numbers of blue-MS and red-MS stars in NGC 1866, which accounts for the presence of binaries among red-MS and blue-MS stars. Since Milone and collaborators show that the two methods provide nearly identical results, for simplicity, we defer the analysis of binaries to forthcoming work.
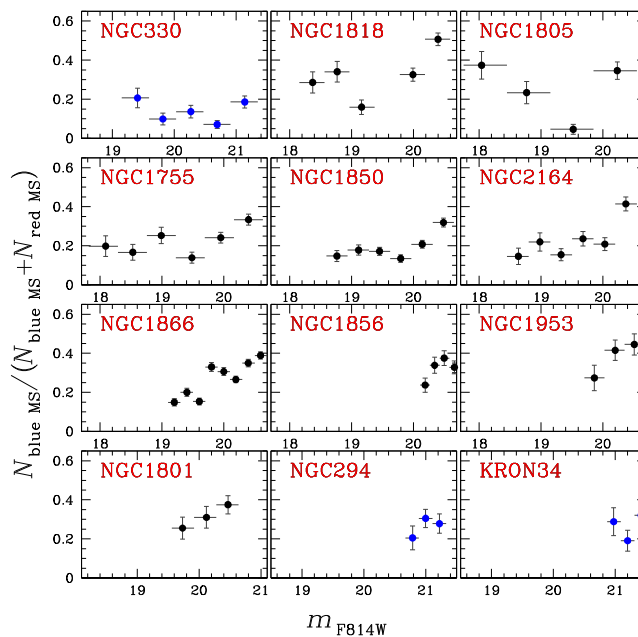
Figure 14. Fraction of blue-MS stars with respect to the overall number of MS stars as a function of the observed *F814W* magnitude.
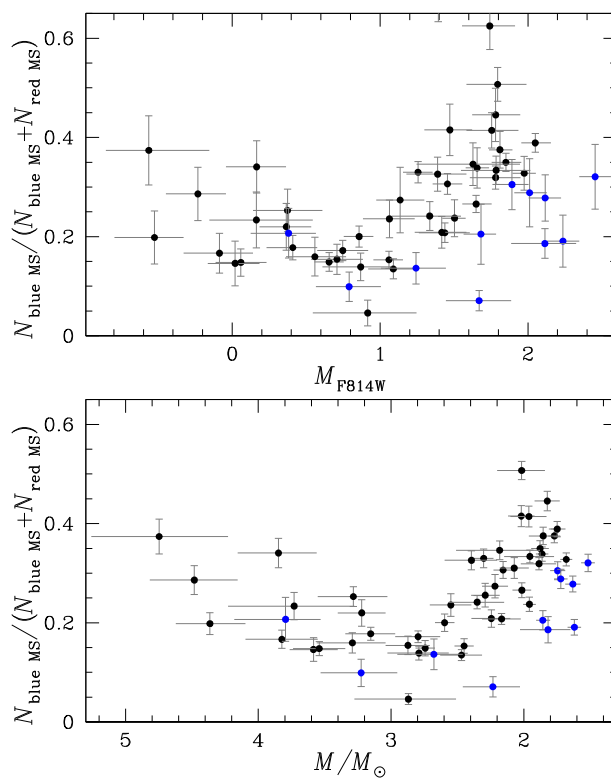

Figure 15. Fraction of blue-MS stars with respect to the overall number of MS stars as a function of the absolute *F814W* magnitude (upper panel) and of the stellar mass (lower panel). Data for the three SMC clusters are represented with blue dots.

The results are illustrated in Fig. 14, where for each cluster we plot the fraction of the blue-MS stars with respect to the total number of MS stars derived in distinct *F814W* magnitude bins as a function of the mean magnitude of all the MS stars in that bin. To compare results from different clusters, in Fig. 15 we plot the fraction of blue-MS stars as a function of the absolute *F814W* magnitude (upper panel) and of the stellar mass (lower panel).

We find that all the LMC clusters follow a similar trend. The fraction of blue-MS stars with respect to the total number of MS stars reaches its maximum value of ~ 0.4 among faint stars with masses of $\sim 1.7\,\mathcal{M}_\odot$ and drops to ~ 0.15 around $\sim 2.8\,\mathcal{M}_\odot$. In the young clusters
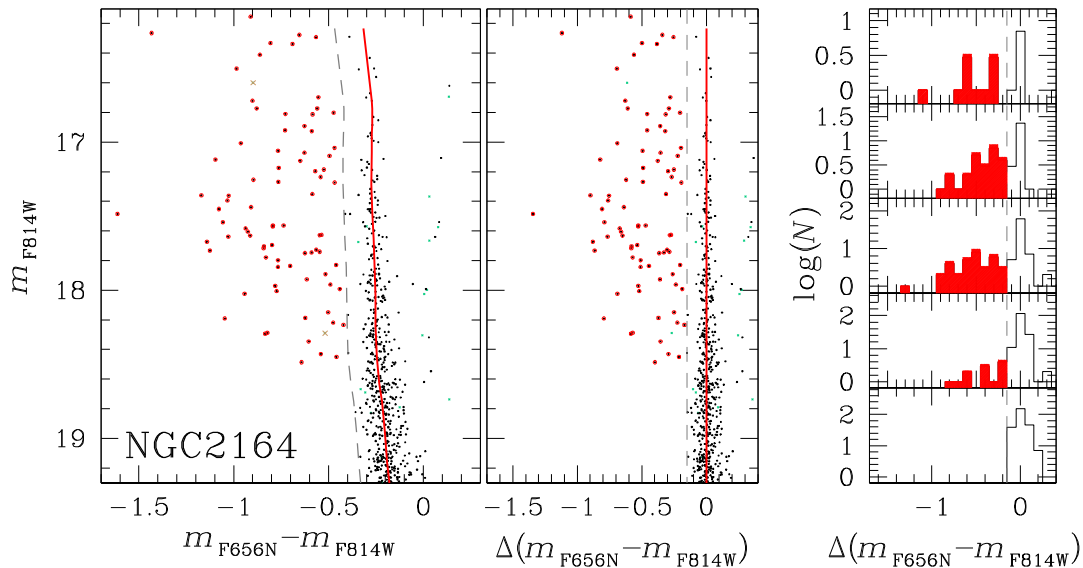
Figure 16. Method to estimate the fraction of stars with Hα emission in NGC 2164. The left-hand panel reproduces the m_{F814W} versus $m_{F656N} - m_{F814W}$ CMD of Fig. 3 with the fiducial line of non-emitter stars represented in red. The left-hand panel shows the verticalized m_{F814W} versus $\Delta(m_{F656N} - m_{F814W})$ diagram, while the right-hand panels show the $\Delta(m_{F656N} - m_{F814W})$ histogram distribution for stars in five magnitude intervals. The vertical dashed lines plotted in the left-hand and middle panels are used to separate candidate Be stars from the remaining MS stars. Candidate Hα emitters are marked with red open dots, while the areas of the corresponding histogram distribution are coloured in red.

(age $\lesssim$ 100 Myr), which host massive MS stars, namely NGC 1818, NGC 1805, NGC 1755, NGC 1850, and NGC 2164, the percentage of blue-MS stars is constant or even seems to increase towards higher masses.

The three SMC clusters are represented with blue dots in Fig. 15 and share a similar trend to LMC clusters but seem to host a lower fraction of blue-MS stars. This fact is particularly evident in NGC 330, which is the youngest analysed SMC cluster, where the fraction of blue-MS stars is almost constant along the entire analysed interval of mass.

7 STARS WITH Hα EMISSION

As shown in Figs 2–6, the five youngest analysed clusters for which photometry in the *F656N* band is available, namely NGC 330, NGC 1805, NGC 1818, NGC 1850, and NGC 2164, host a large number of bright MS stars with $m_{F656N} - m_{F814W}$ colours bluer than the bulk of MS stars by more than 1 mag. Such low $m_{F656N} - m_{F814W}$ colours, which involve stars only around the MSTO, are likely due to strong Hα emission of Be stars.

In contrast, a visual inspection of the m_{F814W} versus $m_{F656N} - m_{F814W}$ CMD of NGC 1856 plotted in Fig. 4 reveals that this cluster does not host MS stars with a strong $m_{F656N} - m_{F814W}$ colour difference from the majority of MS stars (see also Correnti et al. 2015). Nevertheless, the colour and magnitude distribution of stars around the MSTO is broadened with a tail of stars with bluer $m_{F656N} - m_{F814W}$ values than the bulk of MS stars with the same luminosity. A similar conclusion comes from the analysis of the m_{F814W} versus $m_{F625W} - m_{F656N}$ diagram by Bastian et al. (2017).

In the other clusters older than $\sim$100 Myr, namely NGC 1953, NGC 1801, NGC 294, and KRON 34, the upper MS exhibits a wider $m_{F656N} - m_{F814W}$ colour than what we expect from observational errors alone. This fact suggests that weak Hα emitters are likely present in all clusters younger than $\sim$600 Myr. In the following, we analyse the $m_{F656N} - m_{F814W}$ colour and the m_{F814W} magnitude distribution of the Hα emitters.

To investigate how the fraction of Be stars with respect to the total number of MS stars changes as a function of the *F814W* magnitude, we used the procedure illustrated in Fig. 16 for NGC 2164. We selected by eye a sample of MS stars in the cluster-field CMD with no evidence for Hα emission and derived the red fiducial line as described in the previous section and shown in the left-hand panel of Fig. 16. This fiducial has been used to generate the verticalized m_{F814W} versus $\Delta(m_{F656N} - m_{F814W})$ diagram plotted in the middle panel of Fig. 16. All the stars in both the cluster and the reference fields with $\Delta(m_{F656N} - m_{F814W}) < 0.15$ mag are considered as candidate stars with strong emission in Hα.

This procedure has been applied to all the clusters where the observational error in the $m_{F656N} - m_{F814W}$ colour for stars with possible Hα emission is smaller than 0.037 mag, including the five clusters younger than $\sim$100 Myr with available *F656N* photometry and NGC 1856. This choice guarantees that the selected candidate Be stars are unlikely non-emitting MS stars with large photometric uncertainties, as confirmed by AS experiments. We excluded from the analysis the remaining clusters with larger photometric errors.

We derived the $\Delta(m_{F656N} - m_{F814W})$ histogram distributions for stars in five magnitude intervals in both the cluster and reference fields by accounting for the completeness level of each star. The histograms plotted in the right-hand panels of Fig. 16 are calculated as the difference between the histograms of stars in the cluster and reference fields. The shaded-red histograms represent the candidate emitters.
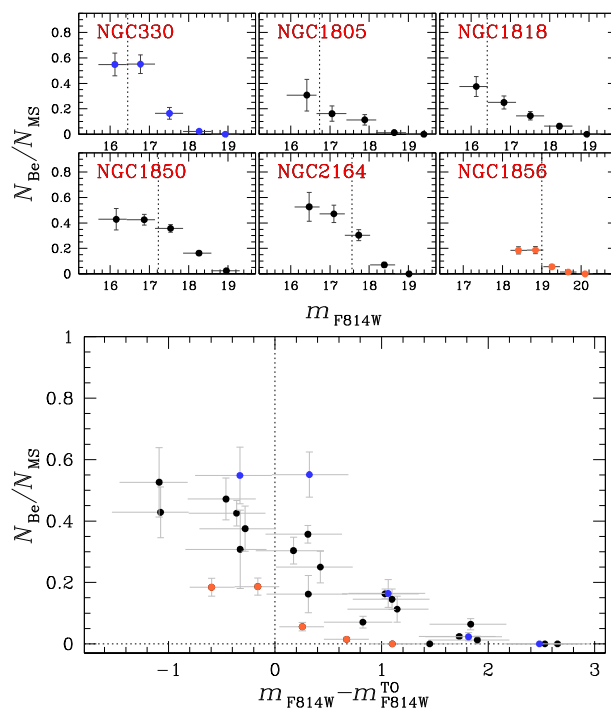
Figure 17. Fraction of stars with Hα emission with respect to the total number of MS stars as a function of the *F814W* magnitude (upper panels) and as a function of the relative magnitude to the turnoff of the red MS (lower panel). The blue points refer to the SMC cluster NGC 330. Orange points indicate the $\sim$300 Myr old LMC cluster NGC 1856. The magnitude of the red-MS turnoff is marked with vertical dotted lines.

The results are illustrated in the upper panels of Fig. 17, where we show for each cluster the fraction of Hα emitters, calculated in five distinct magnitude bins, as a function of the average *F814W* magnitude of all the stars in the corresponding bin. We find that the fraction of Be stars in each cluster reached its maximum around the MSTO, which is indicated with the dotted vertical lines. This conclusion corroborates similar findings by Keller et al. (2000), who derived the luminosity function of Be stars in NGC 330 and in the LMC GCs NGC 1818, NGC 2004, and NGC 2100 and concluded that their fraction of Be stars peaks towards the MS turnoff (see also Iqbal & Keller 2013).

To better compare results from different clusters, we calculated the difference between the average magnitude of stars in the different bins and the magnitude of the red MSTO, m_{F814W}^{TO}, and plotted in the lower panel of Fig. 17 the fraction of Hα emitters as a function of $m_{F814W} - m_{F814W}^{TO}$.

We find that the ratio between the number of strong Hα emitters and the number of MS stars follows similar trends in the analysed clusters. It is maximal above the turnoff, and monotonically decreasing to zero around $m_{F814W} - m_{F814W}^{TO} \sim 2.0$. There is no evidence for Hα emitters with fainter luminosities. In NGC 330, NGC 1818, NGC 2164, and NGC 1850, the emitters comprise up to 40–55 per cent of MS stars, while in the less massive cluster, NGC 1805, the fraction of Be stars is always smaller than $\sim$0.3. In this context, it should be noticed that in clusters with very high radial velocities the Hα line is redshifted to the edge or even outside the passband of the *F656N* filter. For this reason, we cannot exclude that the small fraction of Be stars with excess in the *F656N* band in NGC 1805 is due to its radial velocity of $\sim$+390 km s^{-1} (Fehrenbach 1974). The oldest cluster analysed in this section, NGC 1856, seems to host a smaller fraction of emitting stars than the other GCs.

The comparison of results in the various clusters reveals whether stars with the same absolute magnitude can be Hα emitters or not depending on their relative luminosity with respect to the MSTO. Indeed, while faint Hα emitters in NGC 1856 have absolute magnitude $M_{F814W} \sim 0.7$, there are no Be stars fainter than $M_{F814W} \sim -0.5$ in NGC 330 and no emitting stars with $M_{F814W} \sim 0.5$ in the other analysed clusters. As a consequence, the Be phenomenon seems connected with the evolution of a star along the MS.

The $m_{F656N} - m_{F814W}$ colour of MS stars is analysed in the upper panels of Fig. 18, where we show that the $\Delta(m_{F656N} - m_{F814W})$ histogram distribution for all the MS stars brighter than $m_{F814W}^{TO} = 1.7$ changes from one cluster to another. In NGC 330, the Hα emitters are peaked around $\Delta(m_{F656N} - m_{F814W}) \sim -1.3$, with only few stars having $\Delta(m_{F656N} - m_{F814W}) \gtrsim -1.0$. In contrast, the H$\alpha$ emitters of NGC 1818 exhibit a rather flat $\Delta(m_{F656N} - m_{F814W})$ distribution.

In NGC 1850, which is the cluster with the largest number of stars with Hα excess, we identify some hints of three peaks of emitting stars around $\Delta(m_{F656N} - m_{F814W}) \sim -1.1$, -0.8, and -0.4. In NGC 2164, the number of Hα emitters increases when moving towards higher values of $\Delta(m_{F656N} - m_{F814W})$. The average value of $\Delta(m_{F656N} - m_{F814W})$ increases when moving from young towards older clusters. The 96th percentile of the $\Delta(m_{F656N} - m_{F814W})$ distribution, $\Delta(m_{F656N} - m_{F814W})_{96}$, which is indicative of the maximum colour distance of Be stars from the MS fiducial, ranges from $\sim$1.6 in NGC 330 to $\sim$0.25 in NGC 1856 and correlates with the cluster age as illustrated in the lower panel of Fig. 18. These results provide empirical evidence that the Hα emission is stronger in the young clusters, where the effective temperature of the Be stars around the MSTO is hotter than that of older clusters.
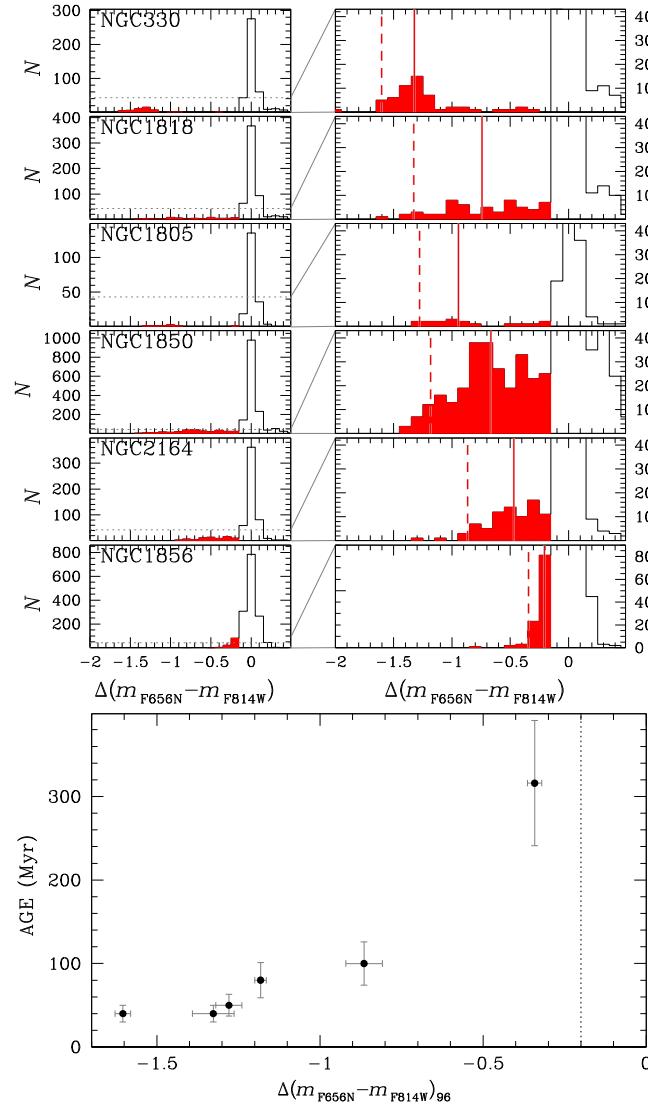
Figure 18. Upper panels: histograms of the $\Delta(m_{F656N} - m_{F814W})$ distribution of stars brighter than $m_{F814W} = 19.3$ (left-hand panels). The right-hand panels are a zoom-in of the left-hand panels. The red-shaded areas indicate the histograms of candidate Hα emitters, while the continuous and the dashed vertical lines mark the values corresponding to the median and the 96th percentile of the $\Delta(m_{F656N} - m_{F814W})$ distribution, respectively. Lower panel: cluster age as a function of the 96th percentile of the $\Delta(m_{F656N} - m_{F814W})$ distribution. The vertical dotted line indicates the adopted separation between candidate stars with strong Hα emission and the other MS stars.

8 SUMMARY AND DISCUSSION

We derived high-precision photometry from UVIS/WFC3 images of 13 young clusters in the LMC and SMC to investigate their multiple stellar populations. The analysed clusters span a wide range of masses from $\sim 10^{3.6}$ to $\sim 10^{5.1}\,\mathcal{M}_\odot$ and ages from ~ 40 Myr to ~ 1 Gyr.

We confirm previous evidence that the MS and the MSTO of NGC 330, NGC 1755, NGC 1805, NGC 1818, NGC 1850, NGC 1856, NGC 1866, and NGC 2164 are not compatible with a simple stellar population (Corrent et al. 2015, 2017; Milone et al. 2015, Milone et al. 2016, Milone et al. 2017a; Bastian et al. 2017; Li et al. 2017a). Moreover, we find that all the analysed clusters exhibit the eMSTO and that all the clusters except for the oldest, NGC 1868, show a split MS.

The fraction of blue-MS stars with respect to the total number of MS stars significantly changes with the stellar luminosity and follows similar trends in the analysed clusters. It reaches its maximum value at $M_{F814W} \sim 1.8$, where the blue MS comprises about ~ 30–40 per cent of the total number of MS stars and monotonically drops down to ~ 15–25 per cent at $M_{F814W} \sim 0.7$. The trend seems reversed and the ratio between the number of blue-MS stars and the total number of MS stars seems increased towards higher luminosity. The red and blue MSs merge brighter than $M_{F814W} \sim 2.0$, thus indicating that there is no evidence for double MSs among stars less massive than $\sim 1.6\mathcal{M}_\odot$ (see also Milone et al. 2017a; D'Antona et al. 2017). NGC 1868, which is the only cluster with no evidence for multiple populations along the MS, is the oldest analysed cluster, and its brightest unevolved MS stars are fainter than $M_{F814W} \sim 1.8$. The fact that all the young clusters follow similar trends suggests that the physical mechanism that is responsible for the split MS is not dependent on the cluster mass.

A possible exception to this notion is NGC 330 in the SMC, which is the youngest analysed cluster, and shows a lower fraction of blue-MS stars than the other clusters in the entire range of magnitudes $M_{F814W} \lesssim 2$. This fact could suggest that all stars form as red-MS stars, and only stars older than a certain age move to the blue MS. However, we note that also the other two analysed SMC clusters, Kron 34 and NGC 294, seem to exhibit a slightly smaller fraction of blue-MS stars than the LMC clusters. Hence, it would be tempting to speculate that either the environment or the cluster metallicity would play a major role in determining the relative numbers of blue-MS and red-MS stars.

Several authors have concluded that a low-metallicity environment such us the SMC hosts a larger fraction of Be stars that higher metallicity environments such us the Milky Way and the LMC do (e.g. Maeder, Grebel & Mermilliod 1999; McSwain & Gies 2005; Iqbal & Keller 2013). A larger sample of clusters is needed to properly investigate these possibilities.

The evidence of multiple populations in all the analysed clusters suggests that the split MS is a common feature in the CMDs of all the star clusters younger than ~1 Gyr and that its presence is closely connected with the evolution of stars brighter than $M_{F814W} \sim 2$. This luminosity corresponds to a stellar mass of $\mathcal{M} \sim 1.6\mathcal{M}_{\odot}$ and corresponds to the MS kink occurring at $T_{\text{eff}} \sim 7500$ K. Such a feature, which also occurs in Galactic open clusters, indicates the onset of envelope convection due to the opacity peak of partial hydrogen ionization (e.g. D'Antona et al. 2002).

Recent work on old Galactic GCs clearly shows that the incidence and the complexity of the multiple-population phenomenon both increase with the cluster mass. In particular, the fraction of second-generation stars with respect to the total number of stars correlates with the mass (Milone et al. 2017b). Our analysis of young clusters reveals that the properties of their multiple sequences analysed in this paper, including the fraction of blue-MS stars with respect to the total number of stars and the stellar rotation rates needed to reproduce the MSs, do not depend on the mass of the host cluster. These facts provide another major difference between the multiple-population phenomena in old and young clusters.

The comparison between the observed CMDs and isochrones from the Geneva data base suggests that the red MS is composed of stars with high rotation rates ($\omega = 0.9\omega_{\text{c}}$), while the blue MS is made of non-rotating or slowly rotating stars in close analogy with what has been suggested for NGC 1856, NGC 1755, NGC 1850, and NGC 1866 (D'Antona et al. 2015; Milone et al. 2016, Milone et al. 2017a; Correnti et al. 2017).

Red-MS stars and the majority of blue-MS stars are consistent with coeval stellar populations. Moreover, the CMDs of all the clusters younger than ~1 Gyr host stars that are fitted by the corresponding slowly rotating isochrones but are younger than the majority of blue-MS stars. These stars have been interpreted by D'Antona et al. (2017) to the braking of the rapidly rotating stars, which end up in having a younger nuclear evolution stage than that of stars slowly rotating from the beginning of their life. D'Antona and collaborators have suggested that the braking could be due to some mechanism of angular momentum loss.

Several papers have shown that young clusters host a large population of Be stars (e.g. Grebel, Richtler & de Boer 1992, 1997; Mazzali et al. 1996; Keller, Wood & Bessell 1999; Bastian et al. 2017; Correnti et al. 2017). The clusters younger than ~600 Myr for which *F656N* photometry is available host a large population of Hα emitters, which are distributed along the upper part of the red MS and the eMSTO. The fact that the Hα emission is associated with the Be phenomenon supports the idea that the red MS is made of fast rotators. The fact that the SMC cluster NGC 330 hosts both a slightly higher fraction of Be stars and a higher fraction of red-MS stars than the studied LMC clusters could suggest that both phenomena depend on the cluster metallicity.

In each of the analysed young clusters, the fraction of Hα emitter stars with respect to the total number of MS stars dramatically changes as a function of magnitude offset from the turnoff. We derived the fraction of Be stars in distinct magnitude intervals and plotted this quantity against the difference between the average *F814W* magnitude of all the stars in each bin and the magnitude of the turnoff of the red MS. In this plane, all the analysed clusters follow similar trends, regardless their mass. The fraction of Be stars is maximal above the MSTO, where the stars with flux excess in the *F656N* include about one-half of the MS stars, and drops to zero about one *F814W* magnitude below the MSTO. These results are consistent with previous evidence that the Be star fraction in a cluster peaks at the MSTO luminosity and decreases with decreasing luminosity (Keller et al. 2000; Iqbal & Keller 2013).

Moreover, the evidence that Hα emitters are present among the upper MS in clusters with different ages, where MSTO stars have different masses, suggests that the stars are not emitters at the formation. The mechanism responsible for the Be phenomenon seems closely connected to the evolution of MS stars instead.

REFERENCES

Anderson J., Bedin L. R., 2010, PASP, 122, 1035

Anderson J., King I. R., 2006, Instrument Science Report ACS 2006-01

Anderson J. et al., 2008, AJ, 135, 2055

Bastian N., de Mink S. E., 2009, MNRAS, 398, L11

Bastian N. et al., 2017, MNRAS, 465, 4795

Bellini A., Anderson J., Bedin L. R., 2011, PASP, 123, 622

Bellini A., Anderson J., Bedin L. R., King I. R., van der Marel R. P., Piotto G., Cool A., 2017, ApJ, 842, 6

Bertelli G., Nasi E., Girardi L., Chiosi C., Zoccali M., Gallart C., 2003, AJ, 125, 770

Bressan G., Marigo P., Girardi L., Salasnich B., Dal Cero C., Rubele S., Nanni A., 2012, MNRAS, 427, 127

Brownsberger S., Romani R. W., 2014, ApJ, 784, 154

Cardelli J. A., Clayton G. C., Mathis J. S., 1989, ApJ, 345, 245

Choi J., Dotter A., Conroy C., Cantiello M., Paxton B., Johnson B., 2016, ApJ, 823, 102

Conroy C., Spergel D. N., 2011, ApJ, 726, 36

Correnti M., Goudfrooij P., Bellini A., Kalirai J. S., Puzia T., 2014, ApJ, 793, 121

Correnti M., Goudfrooij P., Puzia T. H., de Mink S. E., 2015, MNRAS, 450, 3054

Correnti M., Goudfrooij P., Bellini A., Kalirai J. S., Puzia T. H., 2017, MNRAS, 467, 3628

Cutri R. M. et al., 2013, VizieR Online Data Catalog, 2328

D'Antona F., Montalbán J., Kupka F., Heiter U., 2002, ApJ, 564, L93

D'Antona F., Di Criscienzo M., Decressin T., Milone A. P., Vesperini E., Ventura P., 2015, MNRAS, 453, 2637

D'Antona F., Milone A. P., Tailo M., Ventura P., Vesperini E., di Criscienzo M., 2017, Nature Astron., 1, 0186

Dotter A., 2016, ApJS, 222, 8

Dupree A. K. et al., 2017, ApJ, 846, L1

Ekström S. et al., 2012, A&A, 537, A146

Fehrenbach, 1974, A&AS, 13, 173

Gaia Collaboration, Brown A. G. A. et al., 2016, A&A, 595, A2

Gallart C. et al., 2003, AJ, 125, 742

Georgy C., Granada A., Ekstrom S., Meynet G., Anderson R. I., Wyttenbach A., Eggenberger P., Maeder A., 2014, A&A, 566, A21

Gilliland R. L., 2004, Instrument Science Report ACS 2004-01

Gilliland R. L., Rajan A., Deustua S., 2010, Space Telescope WFC Instrument Science Report 2010-10

Glatt K. et al., 2008, AJ, 136, 1703

Goudfrooij P., Puzia T. H., Chandar R., Kozhurina-Platais V., 2011, ApJ, 737, 4

Goudfrooij P. et al., 2014, ApJ, 797, 35

Goudfrooij P., Girardi L., Correnti M., 2017, ApJ, 846, 22

Grebel E. K., 1997, A&A, 317, 448

Grebel E. K., Richtler T., de Boer K. S., 1992, A&A, 254, L5

Iqbal S., Keller S. C., 2013, MNRAS, 435, 3103

Keller S. C., Wood P. R., Bessell M. S., 1999, A&AS, 134, 489

Keller S. C., Bessell M. S., Da Costa G. S., 2000, AJ, 119, 1748

Keller S. C., Mackey A. D., Da Costa G. S., 2011, ApJ, 731, 22

Kiminki M. M., Smith N., Reiter M., Bally J., 2017, MNRAS, 468, 2469

Kurucz R. L., 2005, Mem. Soc. Astron. Ital. Suppl., 8, 14

Li C., de Grijs R., Deng L., 2014, Nature, 516, 367

Li C., de Grijs R., Deng L., Milone A. P., 2017, ApJ, 834, 156

Li C., de Grijs R., Deng L., Milone A. P., 2017, ApJ, 844, 119

Mackey A. D., Broby Nielsen P., 2007, MNRAS, 379, 151

Mackey A. D., Broby Nielsen P., Ferguson A. M. N., Richardson J. C., 2008, ApJ, 681, L17

Mackey J., Gvaramadze V. V., Mohamed S., Langer N., 2015, A&A, 573, A10

McLaughlin D. E., van der Marel R. P., 2005, ApJS, 161, 304

McSwain M. V., Gies D. R., 2005, ApJS, 161, 118

Maeder A., Grebel E. K., Mermilliod J. C., 1999, A&A, 346, 459

Marigo P. et al., 2017, ApJ, 835, 77

Marino A. F. et al., 2014, MNRAS, 442, 3044

Martocchia S. et al., 2017, MNRAS, 468, 3150

Mazzali P. A., Lennon D. J., Pasian F., Marconi G., Baade D., Castellani V., 1996, A&A, 316, 173

Meyssonnier N., Azzopardi M., 1993, A&AS, 102, 451

Milone A. P., 2017, in Charbonnel C., Nota A., eds, Proc. IAU Symp. 316, Formation, Evolution, and Survival of Massive Star Clusters. Cambridge Univ. Press, Cambridge, p. 275.

Milone A. P., Bedin L. R., Piotto G., Anderson J., 2009, A&A, 497, 755

Milone A. P. et al., 2012, A&A, 540, A16

Milone A. P., Bedin L. R., Cassisi S., Piotto G., Anderson J., Pietrinferni A., Buonanno R., 2013, A&A, 555, A143

Milone A. P. et al., 2015, MNRAS, 450, 3750

Milone A. P., Marino A. F., D'Antona F., Bedin L. R., Da Costa G. S., Jerjen H., Mackey A. D., 2016, MNRAS, 458, 4368

Milone A. P. et al., 2017a, MNRAS, 465, 4363

Milone A. P. et al., 2017b, MNRAS, 464, 3636

Mowlavi N., Eggenberger P., Meynet G., Ekström S., Georgy C., Maeder A., Charbonnel C., Eyer L., 2012, A&A, 541, A41

Mucciarelli A. et al., 2011, MNRAS, 413, 837

Mucciarelli A., Dalessandro E., Ferraro F. R., Origlia L., Lanzoni B., 2014, ApJ, 793, LL6

Murphy M. T., Bessell M. S., 2000, MNRAS, 311, 741

Niederhofer F., Georgy C., Bastian N., Ekström S., 2015, MNRAS, 453, 2070

Piatti A. E., Cole A., 2017, MNRAS, 470, L77

Popescu B., Hanson M. M., Elmegreen B. G., 2012, ApJ, 751, 122

Rivinius T., Carciofi A. C., Martayan C., 2013, A&AR, 21, 69

Sabbi E. et al., 2016, ApJS, 222, 11

Sbordone L., Bonifacio P., Castelli F., 2007, in Kupka F., Roxburgh I., Chan K., eds, Proc. IAU Symp. 239, Convection in Astrophysics. Cambridge Univ. Press, Cambridge, p. 71

Wilson C. P., 1975, AJ, 80, 175

Yang W., Meng X., Bi S., Tian Z., Li T., Liu K., 2011, ApJ, 731, LL37

Yang W., Bi S., Meng X., Liu Z., 2013, ApJ, 776, 112

APPENDIX. DISCOVERY OF A NEW STAR CLUSTER

We report the serendipitous discovery of a small star cluster in the outskirts of NGC 330. In the following, we will name this object as GALFOR 1, after the project financed by the European Research Council that supports this paper. The three-colour image of the field of view of NGC 330 is provided in the left-hand panel of Fig. A1 and is derived from the combination of the *F656N* (R channel), *F336W* (G channel), and *F225W* (B channel) master frames. The right-hand panels are zoom-ins of the region around GALFOR 1 in the left-hand panel colour image and in the monochromatic *F225W*, *F336W*, *F656N*, and *F814W* bands.

The cluster is clearly visible on the *F814W* image, and the most prominent feature of the *F656N* image is the nebula that surrounds it. The presence of an overdensity of stars corresponding to the position of the nebula is confirmed by the analysis illustrated in the upper left-hand panel of Fig. A2, where we show the density map of stars brighter than $m_{F814W} = 25.5$ in a region south-east of NGC 330. In
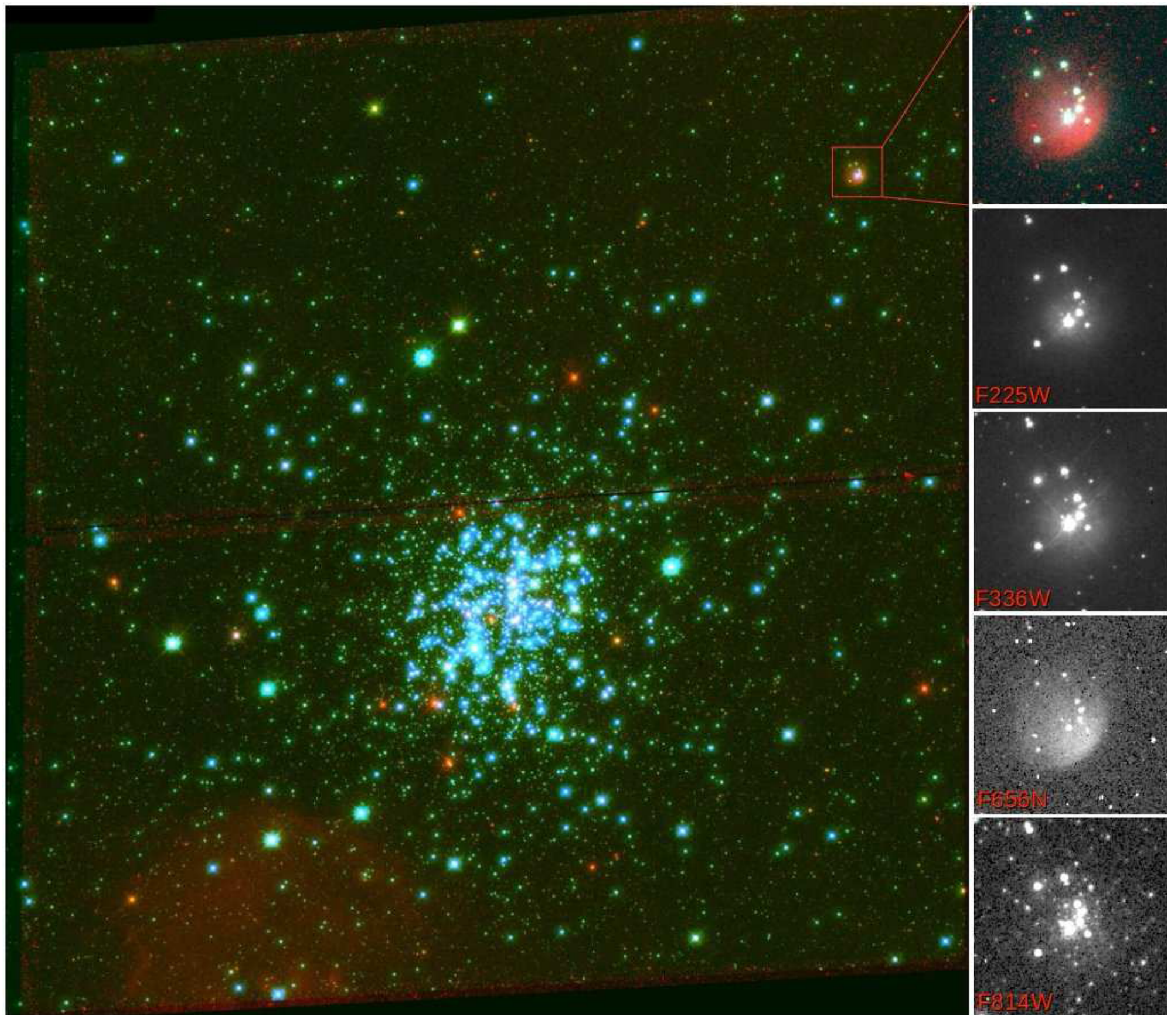

Figure A1. Three-colour image of NGC 330 (left-hand panel). The right-hand panels are zoom-ins of the region around the cluster GALFOR 1, which we have identified in this work. From the top to bottom, we show the three-colour image and images in the *F225W*, *F336W*, *F656N*, and *F814W* bands. South is up and east is on the right.
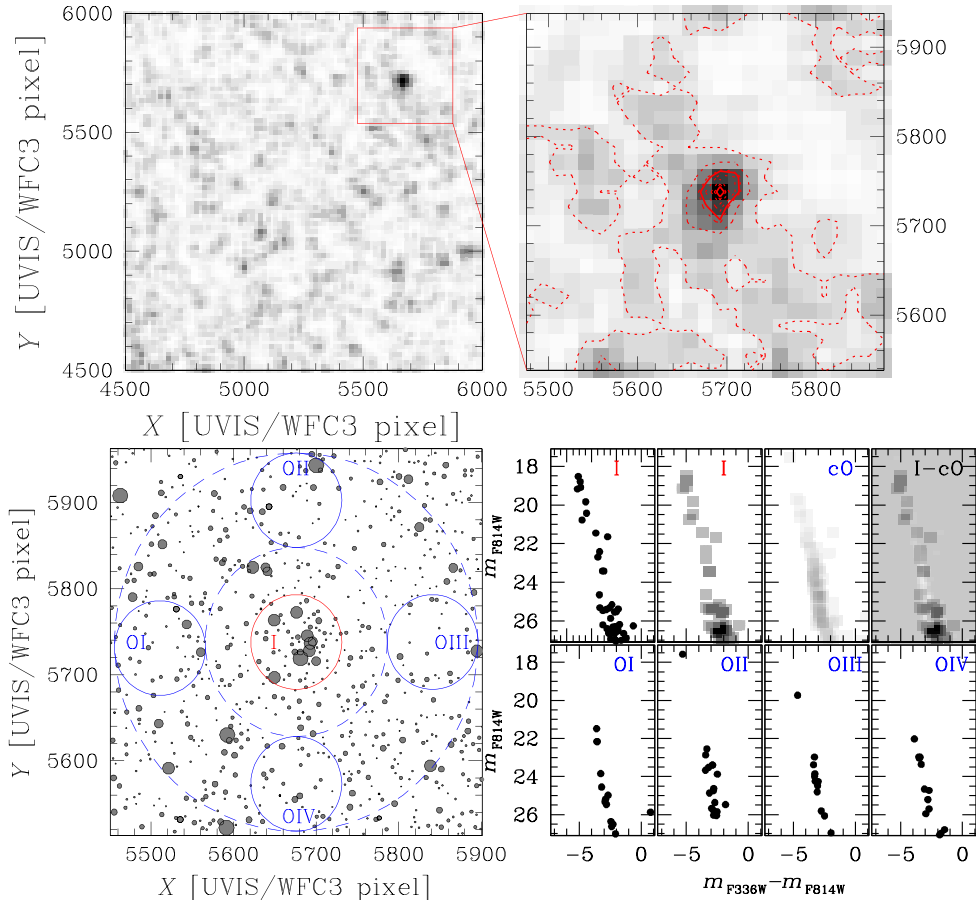
Figure A2. Map of stellar density for stars in a field of 1500×1500 UVIS/WFC3 pixels (1.0 × 1.0 arcmin^2) south-east of NGC 330 (upper left-hand panel). The upper right-hand panel shows a zoom-in of the upper left-hand panel plot in a region centred on the newly discovered star cluster. The contours of stellar density are represented with red lines. The lower left-hand panel shows a map of stars around the newly discovered star cluster. The red circle marks the inner field, I, while the region between the two dashed circles is indicated as the outer field. The four subregions of the outer field (OI, OII, OIII, and OIV) are marked with blue-continuous fields. The m_{F814W} versus $m_{F336W} - m_{F814W}$ CMDs of stars in the fields I and OI–OIV are shown in the lower right-hand panels, where we also plotted the Hess diagram of stars in the fields I and O and the Hess diagram of the corresponding difference. See text for details.

the upper right-hand panel, we overplot the contours on the density map and infer from the contours the position of the cluster centre: RA = 00:56:38.6 Dec. = −72:28:23.7, J2000.

The lower left-hand panel of Fig. A2 shows a map of all the stars brighter than $m_{F814W} = 25.5$ around GALFOR 1. We defined a circle with a radius of 2 arcsec centred on GALFOR 1, which includes most of the cluster members. Moreover, we derived a concentric circular annulus, with an inner and outer radius of 4 and 8 arcsec, respectively, which includes only field stars. The regions within the inner circle and the outer region within the annulus are indicated as the I and O regions, respectively. We also delimit with blue circles four subregions, namely OI–OIV, within the field O with the same area as the field I.

The m_{F814W} versus $m_{F336W} - m_{F814W}$ CMDs of stars in the fields I and OI–OIV are plotted in the lower right-hand panels, which confirm that the field I host a larger number of stars than the surrounding regions. We also show the Hess diagrams of stars in the fields I and O. To properly compare their stellar densities, we multiplied the density of stars in the field O by a constant, $c = 1/12$, which corresponds to the ratio between the areas of the fields O and I. We find that the difference between the stellar density in the field I and the stellar density in the field O multiplied by the constant c is significantly larger than zero, as demonstrated by the corresponding Hess diagram plotted in Fig. A2. These facts demonstrate that the overdensity of stars in the inner field is real and is due to the presence of a small young star cluster.

In their catalogue of H α emission-line stars and small nebulae in the SMC, Meyssonnier & Azzopardi (1993, hereafter MA93) marked at the cluster position an emission-line star, MA93-952, in close analogy with Murphy & Bessell (2000, see their table 1, line 150). The *F656N* photometry analysed in our work shows no evidence of emitting stars in this cluster. As a matter of fact, the *HST* multiband images reveal that GALFOR 1 is immersed in a diffuse nebula with both a reflection and an emission component.

The reflection component, made of scattered starlight by dust, is prominent in the *F225W* and *F336W* filters, where it appears virtually spherical in shape. That a significant amount of interstellar dust is indeed present in the cluster is further supported by the corresponding *WISE* images, which reveal at that position a (clearly not resolved) point source of magnitudes $m_{W1} = 14.454 \pm 0.028$, $m_{W2} = 14.383 \pm 0.039$, $m_{W3} = 9.615 \pm 0.032$, and $m_{W4} = 6.625 \pm 0.057$ (Cutri et al. 2013). The derived infrared excess would thus indicate the presence of moderately cold dust grains at temperature $T_{dust} \lesssim 150$ K.

The H α-emission component, as from the *F656N* filter, appears with a characteristic fan-like shape whose sharp edge is reminiscent of a stellar wind bow-shock (Brownsberger & Romani 2014). The star responsible for the ionization of the interstellar gas is likely the brightest star of the cluster: If our assumption about the presence of a bow shock was correct, then it would imply a supersonic velocity between the star itself and the surrounding ambient medium. In that case, the bow-shock orientation may even be taken as the direction of the star proper motion.

Nevertheless, without further data and a dedicated analysis, we are not in the position of distinguishing whether the bow-shock orientation and morphology are the result of the stellar motion of the local gas dynamics or of density gradients (Kiminki et al. 2017); nor we can confidently exclude the possibility that what we are seeing is actually an interstellar bubble within an H II region that surrounds slowly moving stars (Mackey et al. 2015).

A forthcoming paper will be dedicated to address this and other issues, and to provide a better characterization of this newly discovered SMC star cluster.

[1]*Dipartimento di Fisica e Astronomia 'Galileo Galilei', Univ. di Padova, Vicolo dell'Osservatorio 3, I-35122 Padova, Italy*

[2]*Research School of Astronomy and Astrophysics, Australian National University, Canberra, ACT 2611, Australia*

[3]*Istituto Nazionale di Astrofisica – Osservatorio Astronomico di Roma, Via Frascati 33, I-00040 Monteporzio Catone, Roma, Italy*

[4]*Istituto Nazionale di Astrofisica – Osservatorio Astronomico di Padova, Vicolo dell'Osservatorio 5, I-35122 Padova, Italy*

[5]*Dipartimento di Fisica, Universita' degli Studi di Cagliari, SP Monserrato-Sestu km 0.7, I-09042 Monserrato, Italy*

[6]*Harvard–Smithsonian Center for Astrophysics, 60 Garden Street, Cambridge, MA 02138, USA*

[7]*Departamento de Fisica y Astronomia, Universidad de La Serena, Av. Juan Cisternas 1200 N, La Serena, Chile*

[8]*Instituto de Investigacion Multidisciplinar en Ciencia y Tecnologia, Universidad de La Serena, Raul Bitran 1305, La Serena, Chile*

[9]*Space Telescope Science Institute, 3800 San Martin Drive, Baltimore, MD 21218, USA*

[10] *Department of Physics and Astronomy, Macquarie University, Sydney, NSW 2109, Australia*

[11]*Instituto de Astrofisica de Canarias, E-38200 La Laguna, Tenerife, Canary Islands, Spain*

[12]*Department of Astrophysics, University of La Laguna, E-38200 La Laguna, Tenerife, Canary Islands, Spain*

[13]*Department of Astronomy, Indiana University, Bloomington, IN 47405, USA*

This paper has been typeset from a TEX/LATEX file prepared by the author.